





Constraint on the Ejecta Mass for Black Hole–Neutron Star Merger Event Candidate S190814bv

Kyohei Kawaguchi^{1,2}, Masaru Shibata^{2,3} , and Masaomi Tanaka⁴ 

¹Institute for Cosmic Ray Research, The University of Tokyo, 5-1-5 Kashiwanoha, Kashiwa, Chiba 277-8582, Japan

²Center for Gravitational Physics, Yukawa Institute for Theoretical Physics, Kyoto University, Kyoto, 606-8502, Japan

³Max Planck Institute for Gravitational Physics (Albert Einstein Institute), Am Mühlenberg 1, Potsdam-Golm, D-14476, Germany

⁴Astronomical Institute, Tohoku University, Sendai 980-8578, Japan

Received 2020 February 5; revised 2020 March 22; accepted 2020 March 23; published 2020 April 27

Abstract

We derive the upper limit to the ejecta mass of S190814bv, a black hole–neutron star (BH–NS) merger candidate, through radiative transfer simulations for kilonovae with realistic ejecta density profiles, as well as detailed opacity and heating rate models. The limits to the ejecta mass strongly depend on the viewing angle. For the face-on observations ($\leq 45^\circ$), the total ejecta mass should be smaller than $0.1 M_\odot$ for the average distance of S190814bv ($D = 267$ Mpc), while a larger mass is allowed for the edge-on observations. We also derive the conservative upper limits of the dynamical ejecta mass to be 0.02 , 0.03 , and $0.05 M_\odot$ for the viewing angles $\leq 20^\circ$, $\leq 50^\circ$, and $\leq 90^\circ$, respectively. We show that an *iz*-band observation deeper than 22 mag within 2 days after the gravitational-wave trigger is crucial to detect a kilonova with a total ejecta mass of $0.06 M_\odot$ at a distance of $D = 300$ Mpc. We also show that a strong constraint on the NS mass–radius relation can be obtained if future observations put an upper limit of $0.03 M_\odot$ on the dynamical ejecta mass for a BH–NS event with a chirp mass smaller than $\lesssim 3 M_\odot$ and effective spin larger than $\gtrsim 0.5$.

Unified Astronomy Thesaurus concepts: Gravitational wave astronomy (675); Neutron stars (1108); Black holes (162); Radiative transfer simulations (1967)

1. Introduction

A black hole–neutron star (BH–NS) merger, which is one of the main targets of ground-based gravitational-wave (GW) detectors (LIGO, Aasi et al. 2015; Virgo, Acernese et al. 2015; KAGRA, Kuroda 2010), can be accompanied by an electromagnetic (EM) counterpart if the NS is tidally disrupted (Paczynski 1991; Li & Paczynski 1998). At the onset of tidal disruption, a part of the NS material would be ejected from the system (referred to as the dynamical ejecta; Rosswog 2005; Shibata & Taniguchi 2008; Etienne et al. 2009; Lovelace et al. 2013; Foucart et al. 2014, 2019; Kawaguchi et al. 2015, 2016; Kyutoku et al. 2015, 2018). Subsequently, additional ejecta would be launched from the accreting torus around the remnant BH, driven by amplified magnetic fields or effective viscous heating due to magnetic turbulence (referred to as the postmerger ejecta; Fernández & Metzger 2013; Metzger & Fernández 2014; Just et al. 2015; Kiuchi et al. 2015; Lippuner et al. 2017; Siegel & Metzger 2017, 2018; Ruiz et al. 2018; Christie et al. 2019; Fernández et al. 2019; Fujibayashi et al. 2020). Such ejected material would be the source of the so-called kilonova, which is an EM transient phenomenon in which the emission is powered by radioactive decays of heavy r-process elements synthesized in the ejecta (Li & Paczynski 1998; Kulkarni 2005; Metzger et al. 2010; Kasen et al. 2013; Tanaka & Hotokezaka 2013; Tanaka et al. 2014).

The mass of the dynamical and postmerger ejecta can be either higher or lower than that formed in an NS–NS merger, depending strongly on binary parameters such as the NS mass, BH mass, NS radius, and BH spin (Rosswog 2005; Shibata & Taniguchi 2008; Etienne et al. 2009; Lovelace et al. 2013; Kyutoku et al. 2015; Foucart et al. 2018). It is worth noting that tidal disruption of the NS does not always occur for a BH–NS merger, particularly for cases in which the BH mass is large or

the BH spin or NS radius are small (see, e.g., Foucart et al. 2018). For such a case, no EM counterparts (emitted after merger) will accompany the detection of GWs from a BH–NS merger (however, see, e.g., Carrasco & Shibata 2020; Most & Philippov 2020 for the possible EM precursors). Thus, the detection or nondetection of the kilonova from a BH–NS merger provides us with important information on the binary parameters complementary to that inferred by the GW data analysis.

On 2019 August 14, advanced LIGO and advanced Virgo reported the detection of GWs from a BH–NS merger, which is referred to as S190814bv, with a significantly low value of false-alarm rate (10^{-25} yr^{-1} ; the LIGO Scientific Collaboration and the Virgo Collaboration 2019). The luminosity distance to the event is estimated to be $D = 267 \pm 52$ Mpc (1σ), and the sky localization is achieved within the area of 23 (5) deg^2 for 90% (50%) confidence. Many groups (e.g., Andreoni et al. 2020; Gomez et al. 2019; Singer et al. 2019; Srivastav et al. 2019; Ackley et al. 2020) performed EM follow-up observations. Although no significant EM counterpart was found, upper limits in nearly the whole sky localization region of the event were obtained by their efforts.

The upper limit to the ejecta mass is discussed in Andreoni et al. (2020), Gomez et al. (2019), and Ackley et al. (2020) based on the upper limits to the EM counterparts. By employing the 1D analytical model of Villar et al. (2017), Gomez et al. (2019) explored the ranges of ejecta mass, velocity, and opacity in which the kilonova emission is consistent with the upper limits obtained by their observation (see Figure 4 in Gomez et al. 2019). Andreoni et al. (2020) employed the 1D kilonova model of Hotokezaka & Nakar (2020) and the 2D kilonova model of Bulla (2019) and Dhawan et al. (2020) and suggested that the total ejecta mass should be less than $0.04 M_\odot$ for the face-on observation or less than

$0.03 M_{\odot}$ for the ejecta opacity $\lesssim 2 \text{ cm}^2 \text{ g}^{-1}$ for $D = 215 \text{ Mpc}$. Ackley et al. (2020) employed the 2D kilonova model of Barbieri et al. (2019) and showed that the total ejecta mass larger than $0.1 M_{\odot}$ is excluded with high confidence. However, there are several remarks for the kilonova models employed in previous works. For the 1D model of Hotokezaka & Nakar (2020) and the 2D model of Barbieri et al. (2019), simplified semianalytical models are employed for radiative transfer with a constant gray opacity. For the 2D radiative transfer model (Bulla 2019; Dhawan et al. 2020), the ejecta model with simplified geometry and heating rate is employed, and the temperature and opacity evolution is given a priori. The temperature and opacity evolution of the ejecta and the radiative transfer effect between the multiple ejecta components with nonspherical geometry are crucial for the quantitative prediction of the kilonova light curves (Kawaguchi et al. 2018, 2020; Bulla 2019; Darbha & Kasen 2020). Thus, while these previous models may give a semiquantitative idea for the constraint, an independent quantitative analysis deserves to be performed in a wide range of ejecta parameter space.

In this paper, we report our study of constraining the ejecta mass of S190814bv by performing the radiative transfer simulations for BH–NS kilonovae with the detailed opacity and heating rate models. In this study, kilonova light curves are calculated by employing the ejecta model motivated by numerical-relativity simulations (e.g., Foucart et al. 2014, 2015, 2019; Metzger & Fernández 2014; Kyutoku et al. 2015, 2018; Wu et al. 2016; Siegel & Metzger 2017, 2018; Christie et al. 2019; Fernández et al. 2019; Fujibayashi et al. 2020) and systematically varying the mass of ejecta components. This paper is organized as follows. The setups for the radiative transfer simulation and the ejecta model employed in this work are described in Section 2. In Section 3, we show the upper limits to the ejecta mass of S190814bv. We compare our results with the previous studies by Andreoni et al. (2020) and Ackley et al. (2020) in Section 4. Implications of future observations are presented in Section 4. An idea to constrain the NS mass–radius relation by joint analysis employing the upper limit to the ejecta mass with the GW parameter estimation is also discussed in Section 4. We summarize this work in Section 5. Throughout the paper, magnitudes are given in the AB magnitude system.

2. Method

2.1. Radiative Transfer Simulation

We calculate the light curves of kilonova models for BH–NS mergers by a wavelength-dependent radiative transfer simulation code (Tanaka & Hotokezaka 2013; Tanaka et al. 2017, 2018; Kawaguchi et al. 2020). The photon transfer is calculated by a Monte Carlo method for given ejecta profiles of density, velocity, and element abundance. The nuclear heating rates are determined by employing the results of r-process nucleosynthesis calculations by Wanajo et al. (2014). We also consider the time-dependent thermalization efficiency following an analytic formula derived by Barnes et al. (2016). Axisymmetry is imposed for the matter profile, such as the density, temperature, and abundance distribution. The ionization and excitation states are calculated under the assumption of local thermodynamic equilibrium by using the Saha ionization and Boltzmann excitation equations. Special-relativistic effects on photon transfer and light travel time effects are fully taken into account.

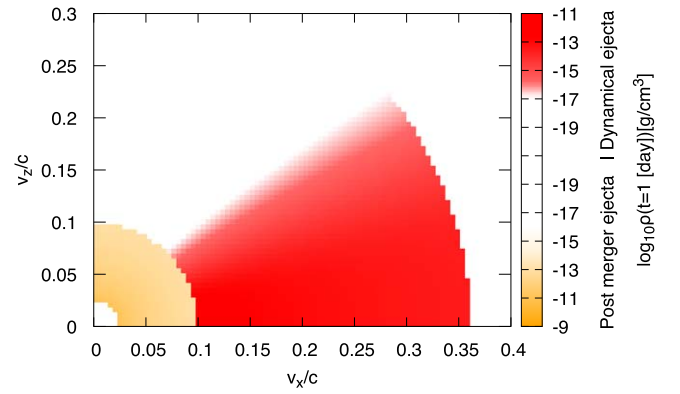


Figure 1. Ejecta density profile employed in the radiative transfer simulation. The density profile for $M_d = M_{\text{pm}} = 0.02 M_{\odot}$ is shown as an example. The red and orange regions denote the dynamical and postmerger ejecta, respectively. Homologous expansion of the ejecta and axisymmetry around the rotational axis (z -axis) are assumed in the simulation.

For photon–matter interaction, we consider bound–bound, bound–free, and free–free transitions and electron scattering for a transfer of optical and infrared photons (Tanaka & Hotokezaka 2013; Tanaka et al. 2017, 2018). The formalism of the expansion opacity (Eastman & Pinto 1993; Kasen et al. 2006) and the updated line list calculated in Tanaka et al. (2019) are employed for the bound–bound transitions. The line list is constructed by an atomic structure calculation for the elements from $Z = 26$ to 92 and supplemented by Kurucz’s line list for $Z < 26$ (Kurucz & Bell 1995), where Z is the atomic number. In particular, we restrict the line list for the transitions of which $\ln(g_l f_l)$ is larger than -2.5 to reduce the computational cost, where g_l and f_l denote the statistical weight and the oscillator strength of the transition, respectively. By this prescription, the line list includes $\approx 7 \times 10^6$ lines. We find the *griz*-band emission obtained by employing this restricted line list to be uniformly brighter by $\approx 0.2 \text{ mag}$ than those employing the line list with $\ln(g_l f_l) > -3$. While we should note that uncertainties in the opacity table, heating rate, and ejecta profile could be larger than this prescription, the brightness of the model light curves shown in this paper is reduced by 0.2 mag to correct this effect.

2.2. Ejecta Profile

Axisymmetric homologously expanding ejecta models that consist of the dynamical ejecta with nonspherical geometry and the postmerger ejecta with spherical geometry are employed in this work (see Figure 1).⁵ As in our previous study (Kawaguchi et al. 2020), we employ the following density profile for the BH–NS ejecta models motivated by the results of numerical-relativity simulations (Foucart et al. 2014; Kyutoku et al. 2015; Siegel & Metzger 2017, 2018; Christie et al. 2019; Fernández et al. 2019; Fujibayashi et al. 2020):

$$\rho \propto \begin{cases} r^{-3} & , 0.025 c \leq r/t \leq 0.1 c \\ \tilde{\Theta}(\theta) r^{-2} & , 0.1 c \leq r/t \leq 0.36 c \end{cases}, \quad (1)$$

⁵ We note that the dynamical ejecta could exhibit nonaxisymmetric morphology in reality (Foucart et al. 2014; Kyutoku et al. 2015).

where $\tilde{\Theta}(\theta)$ is given by

$$\tilde{\Theta}(\theta) = \frac{1}{1 + \exp[-20(\theta - 1.2 \text{ [rad]})]}, \quad (2)$$

and θ is the angle measured from the axis of symmetry. In this model, the dynamical and postmerger ejecta distribute from 0.1 to 0.36 c and from 0.025 to 0.1 c , respectively. The normalization of the density profile is determined so that the dynamical and postmerger ejecta masses are set to be the assumed values M_d and M_{pm} , respectively. The outer edge of the dynamical ejecta ($r/t = v_{d,\text{max}} = 0.36 c$) is determined from the condition that its average velocity defined by $v_{d,\text{ave}} = \sqrt{2E_{K,d}/M_d}$ is 0.25 c , where $E_{K,d}$ is the kinetic energy of the dynamical ejecta (Foucart et al. 2014; Kyutoku et al. 2015). The average velocity of the postmerger ejecta is set to be 0.06 c following the results of numerical-relativity simulations (e.g., Metzger & Fernández 2014; Siegel & Metzger 2017, 2018; Christie et al. 2019; Fujibayashi et al. 2020).⁶

For BH–NS mergers, collisional shock heating or neutrino irradiation in the merger remnant is weak, in contrast to NS–NS mergers (e.g., Fujibayashi et al. 2018); hence, a substantial amount of the ejecta components could have low Y_e values. Taking the prediction obtained by numerical simulations into account (Rosswog et al. 2013; Foucart et al. 2014, 2015, 2019; Metzger & Fernández 2014; Just et al. 2015; Kyutoku et al. 2015, 2018; Wu et al. 2016; Siegel & Metzger 2017, 2018; Christie et al. 2019; Fernández et al. 2019; Fujibayashi et al. 2020), flat Y_e distributions in 0.09–0.11 and 0.1–0.3 are employed for the element abundances of the dynamical and postmerger ejecta, respectively. We note that the recent study by numerical-relativity simulations for the remnant BH accretion torus system pointed out that the significant amount of postmerger ejecta with high values of Y_e ($\gtrsim 0.3$) may be driven even in the absence of the remnant massive NS if the ejection timescale is as long as $\gtrsim 0.3$ s (Fujibayashi et al. 2020). As we show in Appendix B, tighter upper limits to the ejecta mass are obtained for the postmerger ejecta with such high values of Y_e than the one with low values. Thus, the upper limits to the ejecta mass obtained in this work can be regarded as conservative limits.

Wanajo et al. (2014) pointed out that the spontaneous fissions of ^{266}Cf and $^{259,262}\text{Fm}$ can significantly contribute to the heating rate, particularly for $Y_e < 0.1$. Since we employ the heating rate model of Wanajo et al. (2014), these contributions are fiducially taken into account in our kilonova model. However, it is cautioned that the contribution of the spontaneous fissions to the heating rate is highly uncertain due to the uncertainty in the β -decay and spontaneous fission lifetimes of the parent nuclides (e.g., Wanajo et al. 2014; Wanajo 2018; Zhu et al. 2018). The upper limit to the ejecta mass could depend on whether the contribution of the fission fragments to the heating rate is taken into account or not. Indeed, in our previous paper (Kawaguchi et al. 2020), we show that the fission fragments have a significant contribution to enhancing the brightness of the kilonovae, particularly for

our BH–NS kilonova models. Thus, the radiative transfer calculation is also performed for the models without fission fragments to check how the upper limit could be affected by the uncertainty in the fission fragments.

3. Results

Figure 2 shows the *griz*-band light curves observed from $0^\circ \leq \theta_{\text{obs}} \leq 20^\circ$, $41^\circ \leq \theta_{\text{obs}} \leq 46^\circ$, and $86^\circ \leq \theta_{\text{obs}} \leq 90^\circ$ for the model with $M_d = 0.02$ and $M_{\text{pm}} = 0.02 M_\odot$, where θ_{obs} denotes the angle of the observer measured from the axis of symmetry. In Figure 2, we also show the upper limits to the EM counterparts obtained by DECam (Andreoni et al. 2020), ZTF (Singer et al. 2019), Pan-STARRS, VST, and VISTA (Ackley et al. 2020) covering 70%–97% of the sky localization probability (The LIGO Scientific Collaboration and the Virgo Collaboration 2019). Here, t denotes the day since the merger time. Figure 3 is the same as Figure 2 but for the model with $M_d = 0.02$ and $M_{\text{pm}} = 0.04 M_\odot$. As Figures 2 and 3 indicate, for the models with the same amount of dynamical ejecta, the brightness in the *griz* bands increases as the postmerger ejecta mass increases.

The brightness of the kilonova model depends on the viewing angle in the presence of dynamical ejecta reflecting its nonspherical density profile. As θ_{obs} increases, the emission in the *griz* band becomes faint; hence, the upper limit to the ejecta mass becomes weaker approximately monotonically (see also Figure 4). This is due to the blocking of photons emitted from the postmerger ejecta by the dynamical ejecta (Kasen et al. 2015; Kawaguchi et al. 2018, 2020; Bulla 2019), which is enhanced as θ_{obs} increases, since the density of the dynamical ejecta is high around the equatorial plane.

We find that the upper limit to the z band at 3.43 days after the GW trigger obtained by DECam (Andreoni et al. 2020) and the upper limit to the K band at 9.2–10.5 days from VISTA (Ackley et al. 2020) provide the tightest constraint on the kilonova light curves, which cover 97% and 94% of the sky localization probability (The LIGO Scientific Collaboration and the Virgo Collaboration 2019), respectively. Indeed, we find that the other upper limits are always satisfied as far as the kilonova model is consistent with these upper limits. Thus, in the following, we focus on these upper limits to constrain the ejecta mass. Note that, to obtain conservative results, we adapt 10.5 days as the time of the upper limit to the K band obtained by VISTA (Ackley et al. 2020), since the K -band brightness is decreasing in such phase for the kilonova models studied in this work.

3.1. The Upper Limit to the Total Ejecta Mass

In this subsection, we focus on the upper limit to the total ejecta mass. To derive a conservative result, we first explore how the faintest emission is obtained among the fixed total ejecta mass models. Then, we argue the upper limit to the total ejecta mass based on the models.

The brightness of the emission depends on the ratio between the dynamical and postmerger ejecta mass among the fixed total ejecta mass models. As an illustration, Figures 4 and 5 show the brightness of the z -band emission at $t = 3.43$ days as functions of θ_{obs} and M_{pm} for the models with $M_d + M_{\text{pm}} = 0.06 M_\odot$, respectively. For $\theta_{\text{obs}} \lesssim 45^\circ$, we find that the z -band brightness at $t = 3.43$ days for the models with the same total ejecta mass increases approximately monotonically as the ratio

⁶ We note that the significant amount of ejecta of which the velocity is higher than 0.1 c could be formed in the presence of globally coherent and strong poloidal magnetic fields, although it is not very clear how such magnetic fields are established soon after the onset of merger (Siegel & Metzger 2018; Christie et al. 2019).

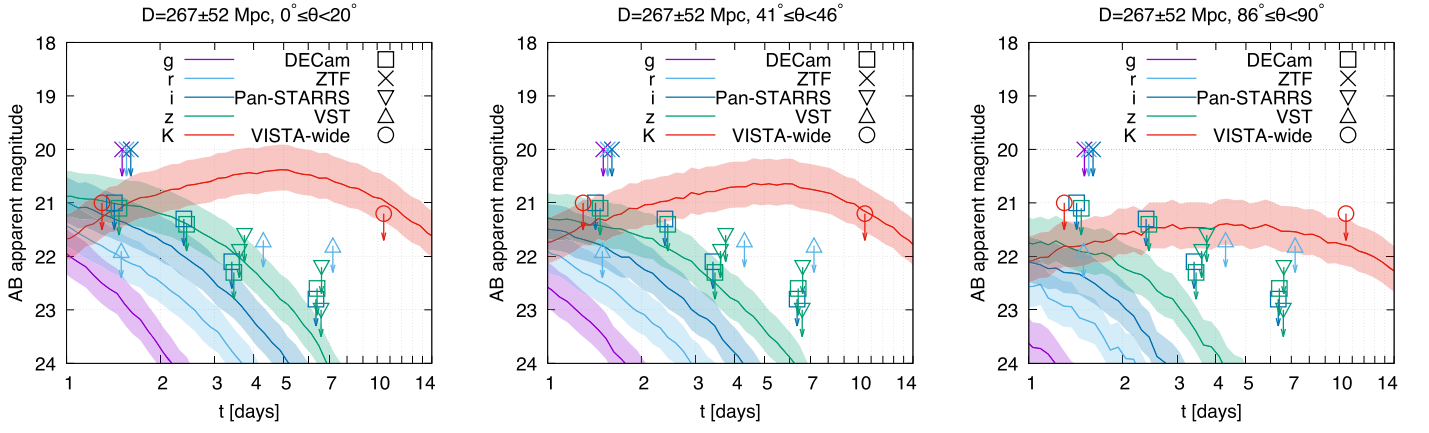


Figure 2. The *griz*-band light curves of a BH–NS kilonova model for $M_d = 0.02$ and $M_{pm} = 0.02 M_\odot$. The shaded regions denote the uncertainty in the brightness due to the error bar of the luminosity distance (The LIGO Scientific Collaboration and the Virgo Collaboration 2019). The upper limits to the EM counterparts obtained by DECcam (Andreoni et al. 2020), ZTF (Singer et al. 2019), Pan-STARRS, VST, and VISTA (Ackley et al. 2020) covering 70%–97% of the sky localization probability (The LIGO Scientific Collaboration and the Virgo Collaboration 2019) are shown. The purple, light blue, blue, green, and red curves and points denote the light curves and upper limits for the *g*-, *r*-, *i*-, *z*-, and *K*-band filters, respectively.

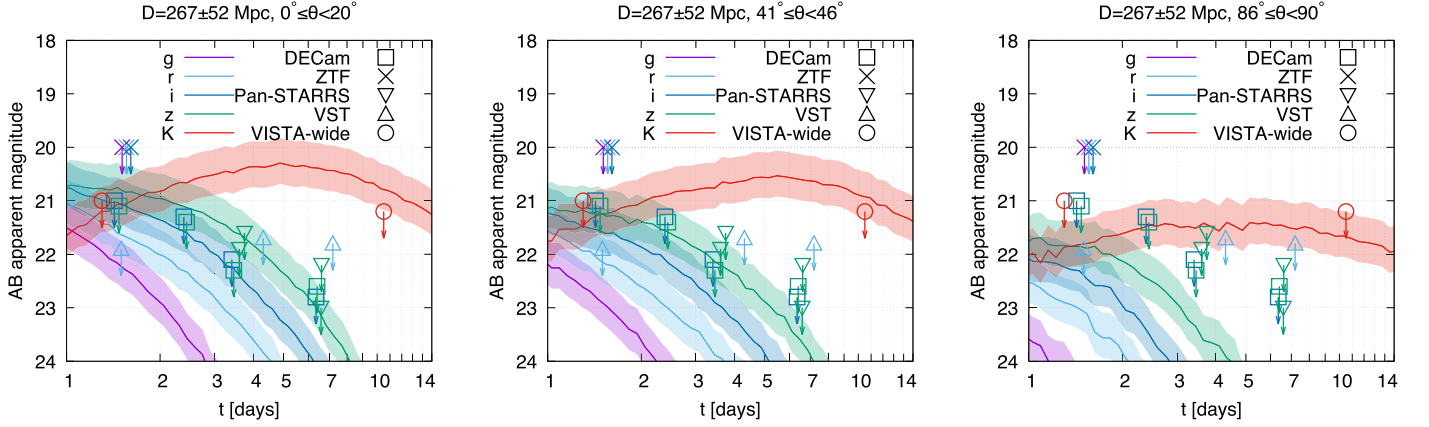


Figure 3. Same as Figure 2 but for the model with $M_d = 0.02$ and $M_{pm} = 0.04 M_\odot$.

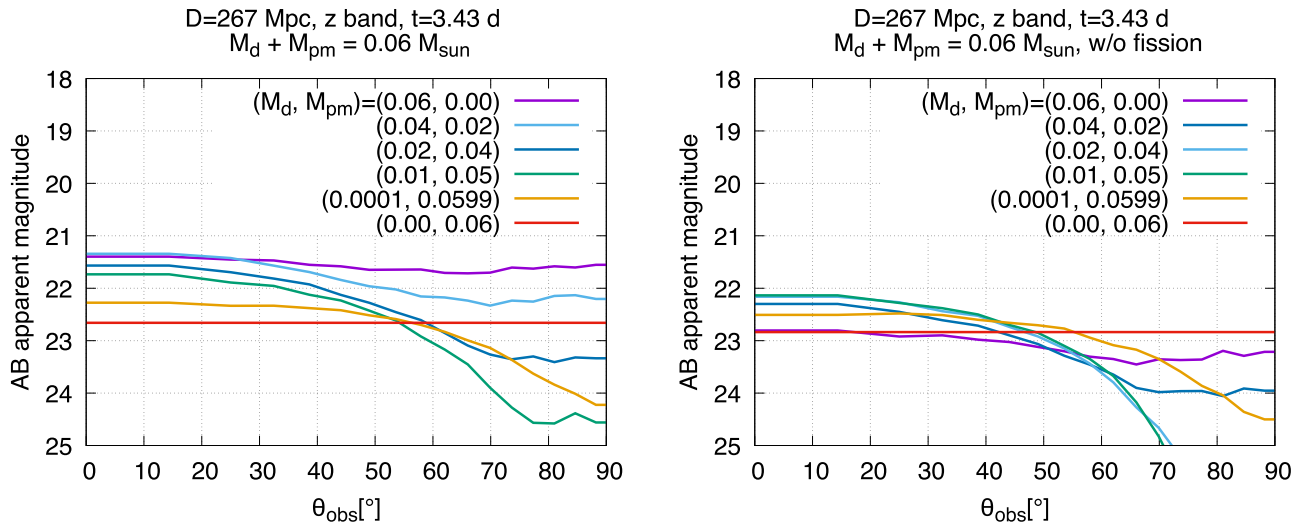


Figure 4. Brightness of the *z*-band emission at $t = 3.43$ days as a function of the viewing angle, θ_{obs} , for several models with $M_d + M_{pm} = 0.06 M_\odot$. The values in the legend denote (M_d, M_{pm}) in units of M_\odot . The left and right panels show the results that take into account and omit the contribution from the fission fragments to the heating rate, respectively. We note that there is no viewing angle dependence for the model with only the spherical postmerger ejecta.

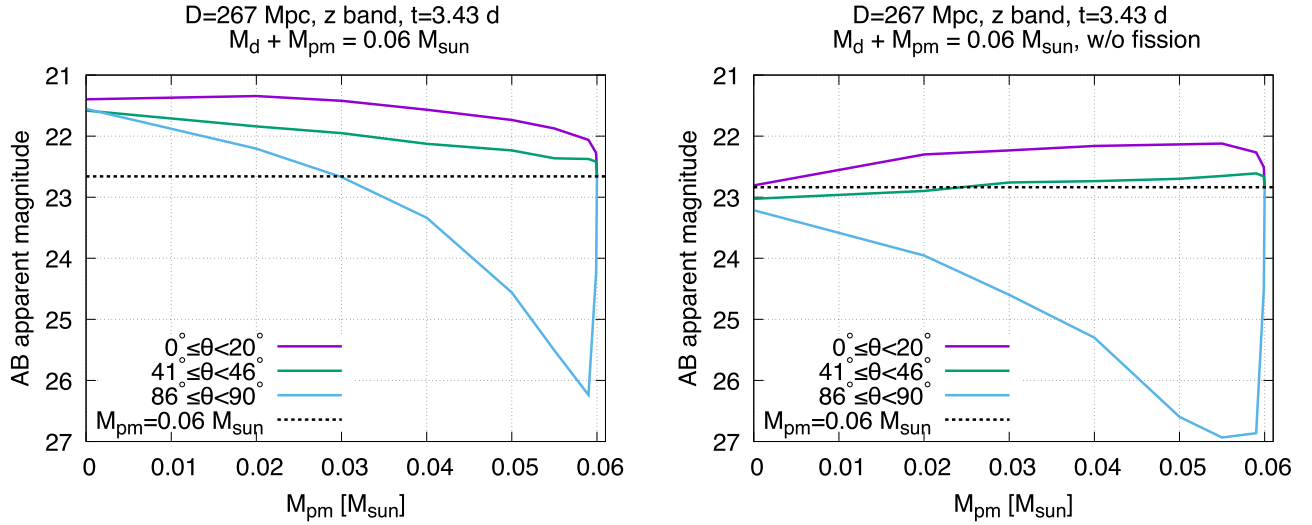


Figure 5. Brightness of the z -band emission at $t = 3.43$ days as a function of M_{pm} for the models with $M_{\text{d}} + M_{\text{pm}} = 0.06 M_{\odot}$. The left and right panels show the results that take into account and omit the contribution from the fission fragments to the heating rate, respectively. The dashed line denotes the brightness for the model with $M_{\text{pm}} = 0.06$ and $M_{\text{d}} = 0.00 M_{\odot}$.

$M_{\text{d}}/M_{\text{pm}}$ increases, and the faintest emission is realized for the model only with the postmerger ejecta if the fission fragment is taken into account. This is mostly due to the fact that the specific deposition rate of thermal photons, which is determined by the radioactive heating rate and thermalization efficiency, is higher for the dynamical ejecta than the postmerger ejecta. We note that the difference in the opacity is also responsible for the difference in the brightness. However, for $\theta_{\text{obs}} \lesssim 45^\circ$, this effect is minor.

In contrast, the dependence of the z -band brightness at $t = 3.43$ days on the ratio $M_{\text{d}}/M_{\text{pm}}$ is more complicated for $\theta_{\text{obs}} \gtrsim 45^\circ$. The emission becomes faint as the ratio $M_{\text{d}}/M_{\text{pm}}$ decreases for $M_{\text{d}} \gtrsim 0.01 M_{\odot}$, but the brightness increases again for $M_{\text{d}} \lesssim 0.001 M_{\odot}$. This is due to the fact that, with the decrease of M_{d} , the emission from the dynamical ejecta becomes less significant, and only its own blocking effect of photons plays a role (Kasen et al. 2015; Kawaguchi et al. 2018, 2020; Bulla 2019). For such a situation, the emission becomes bright as the dynamical ejecta mass decreases.

The dependence of the emission on the ratio $M_{\text{d}}/M_{\text{pm}}$ is different for the case in which the contribution from the fission fragments to the heating rate is omitted. For such cases, the z -band brightness observed from $\theta_{\text{obs}} \lesssim 45^\circ$ at $t = 3.43$ days becomes the brightest for $M_{\text{d}}/M_{\text{pm}} \approx 20\% - 50\%$, and it becomes faint as the ratio increases. Nevertheless, the faintest emission is realized approximately for the model with only the postmerger ejecta for $\theta_{\text{obs}} \lesssim 45^\circ$. The dependence of the z -band brightness on the ratio $M_{\text{d}}/M_{\text{pm}}$ for $\theta_{\text{obs}} \gtrsim 45^\circ$ is qualitatively similar to what is found for the models with the fission fragments. However, the emission is fainter by 1.5 mag than those with the fission fragments, and the model with only the postmerger ejecta always gives the brightest light curve.

We find that the brightness of the K -band emission at $t = 10.5$ days also shows broadly the same dependence on the ratio $M_{\text{d}}/M_{\text{pm}}$ as for the z -band emission at $t = 3.43$ days. For the K -band emission at $t = 10.5$ days, the decrease of the brightness due to the blocking effect is much less significant, and the difference in the emission observed from the polar and equatorial directions is $\lesssim 1.5$ mag.

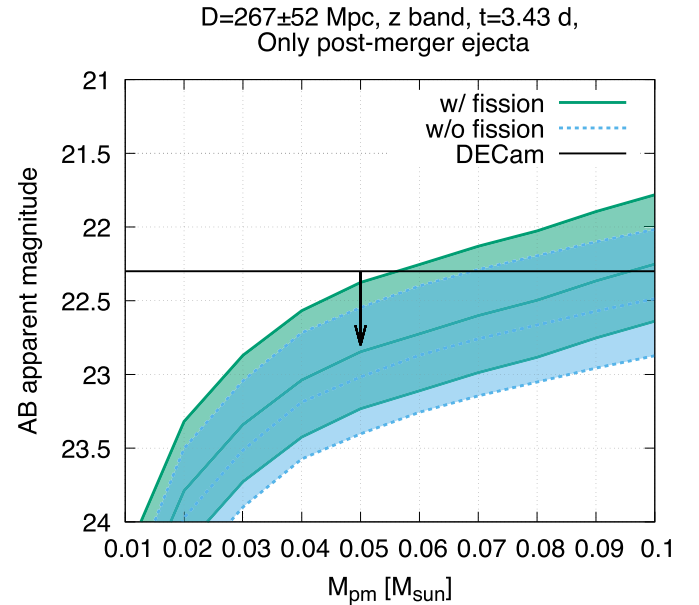


Figure 6. Brightness of the z -band emission at $t = 3.43$ days as a function of ejecta mass for the model with only the postmerger ejecta. The curves plotted at the center of the shaded regions denote the brightness for $D = 267$ Mpc, while the curves plotted at the lower and upper edges denote the brightness assuming $D = 267 \pm 52$ Mpc, respectively (The LIGO Scientific Collaboration and the Virgo Collaboration 2019). The black horizontal line shows the upper limit to the z -band emission at 3.43 days for S190814bv obtained by DECAM (Andreoni et al. 2020). We note that there is no viewing angle dependence for the model with only the spherical postmerger ejecta.

If $\theta_{\text{obs}} \leq 45^\circ$, the model with only the postmerger ejecta provides a conservative upper limit to the total ejecta mass. We find that the upper limit to the z -band emission at 3.43 days provides the tightest constraint for this setup. Figure 6 shows the brightness of the z -band emission at $t = 3.43$ days as a function of ejecta mass for the model with only the postmerger ejecta. For $D \geq 267$ Mpc, only weak upper limits are obtained, and the model with $\lesssim 0.1 M_{\odot}$ is always consistent with the upper limit to the emission. On the other hand, assuming an optimistic distance of 215 Mpc, the upper limit to the emission

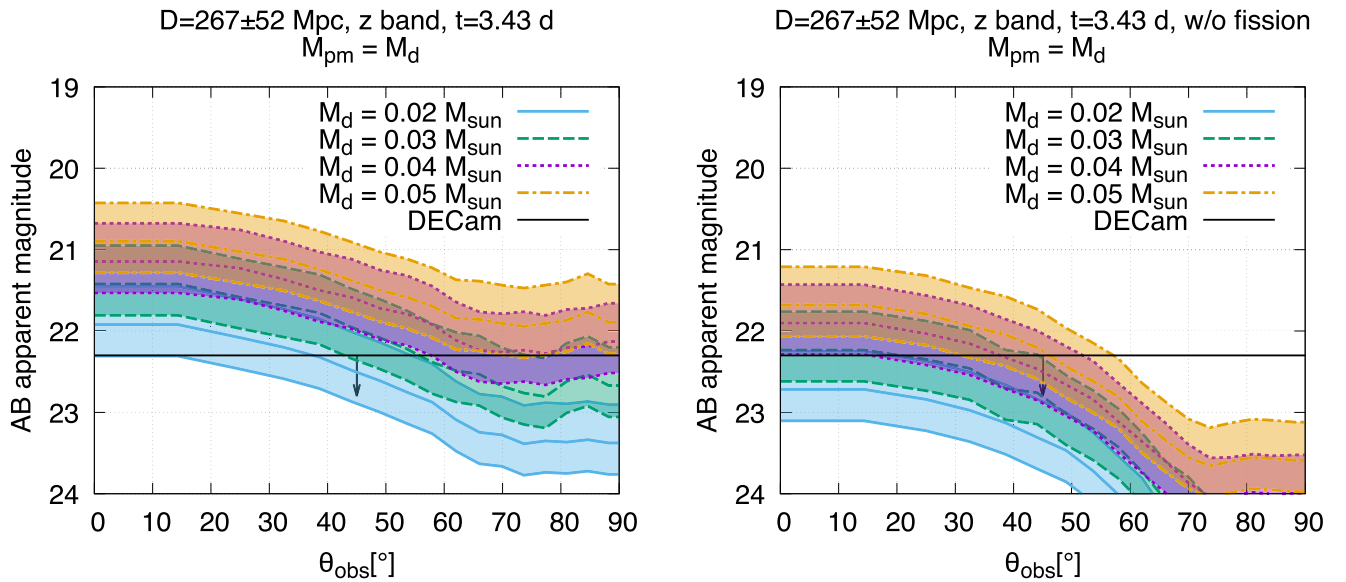


Figure 7. Brightness of the z -band emission at $t = 3.43$ days as a function of viewing angle, θ_{obs} . The left panel shows the light curves for the models with $(M_d, M_{\text{pm}}) = (0.02, 0.02 M_\odot)$; blue solid), $(0.03, 0.03 M_\odot)$; green dashed), $(0.04, 0.04 M_\odot)$; purple dotted), and $(0.05, 0.05 M_\odot)$; orange dotted). The right panel is the same as the left panel but for the models in which the contribution from the fission fragments to the heating rate is omitted. The curves plotted at the center of the shaded regions denote the brightness for $D = 267$ Mpc, while the curves plotted at the lower and upper edges denote the brightness assuming $D = 267 \pm 52$ Mpc, respectively (The LIGO Scientific Collaboration and the Virgo Collaboration 2019). The black horizontal lines in the left and right panels show the upper limits to the z -band emission at 3.43 days for S190814bv obtained by DECcam (Andreoni et al. 2020).

obtained by Andreoni et al. (2020) implies that the total ejecta mass should be less than ≈ 0.06 and $\approx 0.07 M_\odot$ for the models with and without the fission fragments, respectively.

The constraints become much weaker if $\theta_{\text{obs}} \gtrsim 60^\circ$, because the faintest emission for this case is realized in the presence of a fraction of the dynamical ejecta for the case in which the blocking effect of the dynamical ejecta is significant. The z -band emission is suppressed by 1–2 mag more than the case with the same total ejecta mass but only the postmerger ejecta. For a large viewing angle ($\theta_{\text{obs}} \gtrsim 60^\circ$), the upper limit to the K -band emission provides the tightest constraint, since the suppression due to the blocking effect is less significant for the K -band emission. Nevertheless, we find that the total ejecta mass as large as $0.1 M_\odot$ is consistent with the observation, even assuming $D = 215$ Mpc.

3.2. The Upper Limit to the Dynamical Ejecta Mass

In this section, we focus on the upper limit to the dynamical ejecta mass. As shown in the previous subsection, the z -band brightness observed from $\theta_{\text{obs}} \lesssim 45^\circ$ at $t = 3.43$ days increases as the ratio M_d/M_{pm} increases for the fixed total ejecta mass and for the case in which the fission fragments play an important role. This indicates that the obtained upper limit to the emission could be informative to constrain the dynamical ejecta mass. Furthermore, for BH–NS mergers, the connection between the dynamical ejecta mass and the binary parameters, such as the mass of each component, BH spin, and NS radius, is expected to be predicted relatively more accurately by numerical-relativity simulations than the postmerger or dynamical ejecta for NS–NS mergers (Hotokezaka et al. 2013; Kyutoku et al. 2015; Dietrich & Ujevic 2017; Foucart et al. 2018). This is because the dynamical ejecta is driven approximately purely by gravitational torque for BH–NS mergers, while shocks and magnetically driven turbulence also play important roles for the others. Thus, the constraint on the

dynamical ejecta mass could be useful for constraining the parameters of observed binaries, as we discuss in Section 4.

Numerical-relativity simulations for BH–NS mergers suggest that the remnant torus (the gravitationally bounded component of the material that remains after the merger) is typically more massive than the dynamical ejecta (e.g., Kyutoku et al. 2015; Foucart et al. 2019). This indicates that a significant amount of the postmerger ejecta would always be accompanied by the massive dynamical ejecta. In fact, for example, numerical-relativity simulations for BH–NS mergers (e.g., Kyutoku et al. 2015; Foucart et al. 2019) show that the mass of the remnant torus is typically larger than the dynamical ejecta mass by a factor of more than 3. Magnetohydrodynamics or viscous hydrodynamics simulations for the BH accretion torus systems (Fernández & Metzger 2013; Metzger & Fernández 2014; Just et al. 2015; Siegel & Metzger 2017, 2018; Christie et al. 2019; Fernández et al. 2019; Fujibayashi et al. 2020) suggest that $\approx 20\%$ – 30% of the remnant torus could be ejected from the system. Hence, the postmerger ejecta mass is likely to be larger than or comparable with the dynamical ejecta mass. In the following, we focus particularly on the models with $M_{\text{pm}} = M_d$. This is because the brightness in the $griz$ bands for a given epoch $\gtrsim 0.3$ days increases monotonically as the postmerger ejecta mass increases for the models with a fixed amount of the dynamical ejecta; thus, the models with $M_{\text{pm}} = M_d$ provide a conservative upper limit to the dynamical ejecta mass for given upper limit to the emission as long as they are focusing on the cases of $M_{\text{pm}} \geq M_d$ (see Appendix A for the upper limit to the dynamical ejecta mass assuming a more conservative setup, $M_{\text{pm}} = 0.5 M_d$).

The left panel of Figure 7 shows the z -band brightness at 3.43 days after the merger as a function of θ_{obs} for the models with $(M_d, M_{\text{pm}}) = (0.02, 0.02 M_\odot)$, $(0.03, 0.03 M_\odot)$, $(0.04, 0.04 M_\odot)$, and $(0.05, 0.05 M_\odot)$, together with the upper limit by DECcam (Andreoni et al. 2020). In the following, we

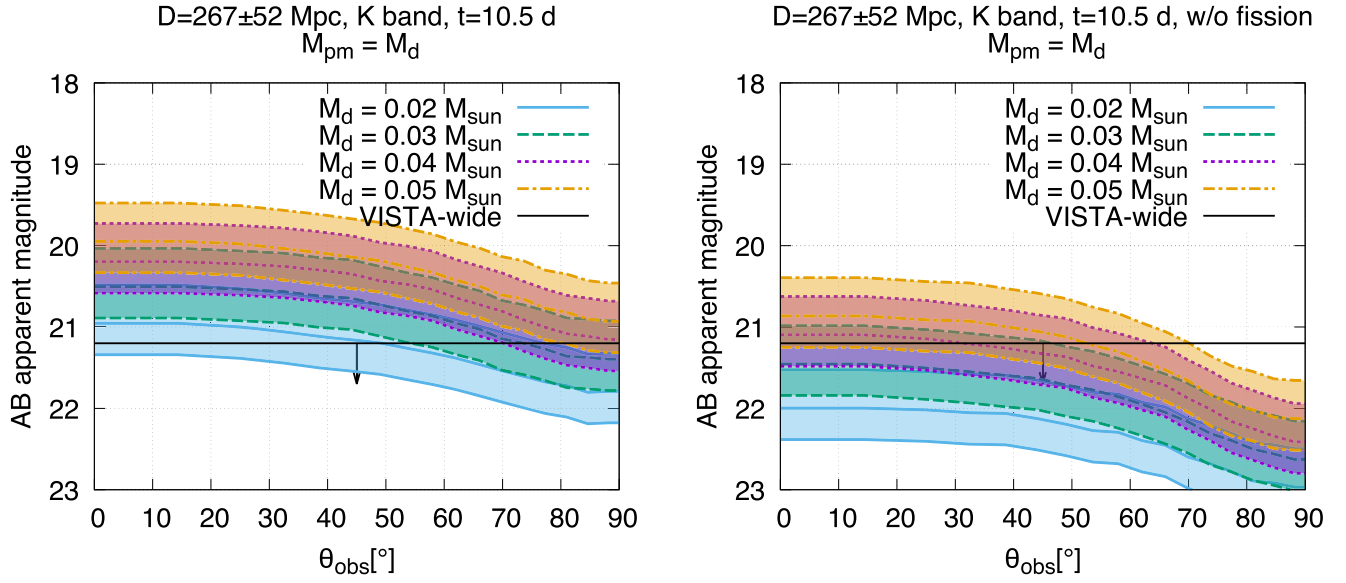


Figure 8. Same as Figure 7 but for the brightness of the K-band emission at $t = 10.5$ days with the upper limit obtained by VISTA (Ackley et al. 2020).

focus on the results assuming $D = 319$ Mpc to obtain conservative upper limits. Here $D = 319$ Mpc is the 1σ far edge of the posterior inferred by the GW analysis (The LIGO Scientific Collaboration and the Virgo Collaboration 2019), and the lower edge of the shaded region in Figure 7 corresponds to the predicted brightness for $D = 319$ Mpc. We note that the estimated distance should depend on the viewing angle, and larger and smaller distances would be favored for the face-on and edge-on observations, respectively, due to the correlation in determining GW amplitude (for example, see Abbott et al. 2020 for the case of GW 190425).

If $\theta_{\text{obs}} \leq 45^\circ$, the emission in the z band at 3.43 days for the model with $(M_d, M_{\text{pm}}) = (0.03, 0.03 M_\odot)$ is brighter than 22.3 mag for the inferred 1σ range of the luminosity distance. This indicates that the ejecta with $M_d = M_{\text{pm}} \geq 0.03 M_\odot$ is unlikely to be driven in S190814bv if $\theta_{\text{obs}} \leq 45^\circ$. For a smaller value of θ_{obs} , the upper limit to the ejecta mass becomes tighter. For $\theta_{\text{obs}} \leq 20^\circ$, the model with $(M_d, M_{\text{pm}}) = (0.02, 0.02 M_\odot)$ is disfavored or only marginally consistent with the upper limit to the z -band emission at 3.43 days. On the other hand, the models with $M_{\text{pm}} = M_d \leq 0.04 M_\odot$ cannot be ruled out if $\theta_{\text{obs}} \gtrsim 60^\circ$. The models with $M_{\text{pm}} = M_d \geq 0.05 M_\odot$ are always disfavored regardless of the viewing angle.

The right panel of Figure 7 is the same as the left panel but for the models in which the contribution from the fission fragments to the heating rate is omitted. The z -band emission becomes fainter by ≈ 1 and ≈ 2 mag for the polar and equatorial direction, respectively, than the results shown in the left panel of Figure 7. The brightness observed from the equatorial direction is affected more significantly than that observed from the polar direction by omitting the fission fragments because it is dominated by the emission from the dynamical ejecta in our models, in which the fission fragments have a large impact on the heating rate. Due to the fainter emission, the upper limit to the ejecta mass is weaker for the models without the fission fragments. If θ_{obs} is larger than 30° , the model with $M_d \geq 0.05 M_\odot$ is consistent with the upper limit to the emission. On the other hand, if θ_{obs} is smaller than 30° , the models with only $M_d \leq 0.04 M_\odot$ are allowed for the assumption with $M_{\text{pm}} \geq M_d$.

Figure 8 is the same as Figure 7 but for the brightness of the K-band emission at $t = 10.5$ days with the upper limit obtained by VISTA (Ackley et al. 2020). The upper limit to the K-band emission provides approximately the same or a weaker constraint on M_d than that to the z band for $\theta_{\text{obs}} \lesssim 45^\circ$ but a slightly tighter constraint for $\theta_{\text{obs}} \gtrsim 45^\circ$ due to a weaker viewing angle dependence. For the model taking the fission fragments into account, $M_d \geq 0.03$ and $0.04 M_\odot$ are disfavored for $\theta_{\text{obs}} \lesssim 50^\circ$ and 70° , respectively. This indicates that the observation in the near-infrared wavelength is useful to detect or constrain the kilonova emission for a large viewing angle.

As a summary, Figure 9 shows the upper limit to the dynamical ejecta mass as a function of viewing angle, θ_{obs} . The figure shows that the upper limit to the dynamical ejecta mass is weaker by a factor of $\approx 2-3$ by omitting the contribution of the fission fragments to the heating rate. Overall, the constraints are not strong enough to indicate particular parameters of the binary.

4. Discussion

4.1. Comparison with the Ejecta Mass Constraints Obtained in Andreoni et al. (2020) and Ackley et al. (2020)

In the work of Andreoni et al. (2020), the upper limit to the ejecta mass is obtained by employing the 1D kilonova models of Hotokezaka & Nakar (2020) and 2D kilonova models of Bulla (2019) and Dhawan et al. (2020). Ackley et al. (2020) also provided the upper limit to the ejecta mass based on the 2D analytical model of Barbieri et al. (2019). In this subsection, we compare their results with ours.

First, we compare our results with those obtained by the 2D kilonova model of Bulla (2019) and Dhawan et al. (2020). For their model, we note the following. (i) The ejecta density profile is simplified by a homogeneously expanding spherical ejecta distributing up to $0.3c$. (ii) The spherical ejecta is divided into the polar and equatorial regions by certain degrees of latitude, and opacity models mimicking the lanthanide-poor and lanthanide-rich material are arranged in these regions, respectively. (iii) The light curves are calculated using a wavelength-dependent Monte Carlo code, while the power-law

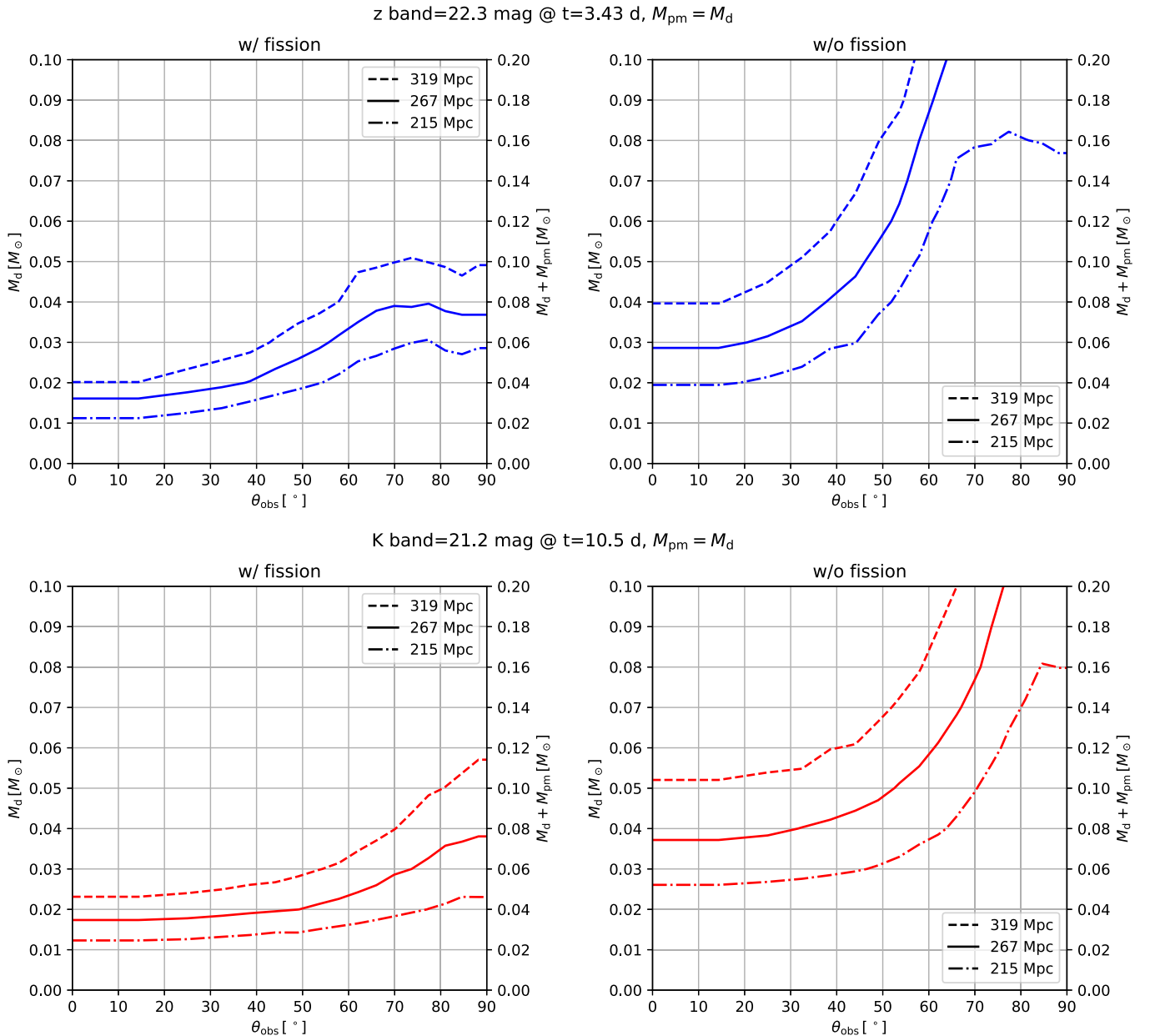


Figure 9. Upper limit to the dynamical ejecta mass, M_d , as a function of viewing angle, θ_{obs} , consistent with the upper limits. The top and bottom panels denote the results for the upper limits to the z -band emission at 3.43 days obtained by DECam (Andreoni et al. 2020) and the K -band emission at $t = 10.5$ days obtained by VISTA (Ackley et al. 2020), respectively. The left and right panels show the results that take into account and omit the contribution from the fission fragments to the heating rate, respectively. The dashed, solid, and dashed-dotted curves denote the upper limits to the dynamical ejecta mass obtained assuming $D = 319$, 267, and 215 Mpc, respectively.

temperature evolution, as well as the time evolution of the opacity, are assumed a priori and uniformly over the whole ejecta. On the other hand, the lanthanide-rich dynamical and postmerger ejecta with the density profile consistent with the numerical-relativity simulations (e.g., Foucart et al. 2014, 2015, 2019; Metzger & Fernández 2014; Kyutoku et al. 2015, 2018; Wu et al. 2016; Siegel & Metzger 2017, 2018; Christie et al. 2019; Fernández et al. 2019; Fujibayashi et al. 2020) are employed, and the temperature and opacity are evolved consistently with the radiative transfer in our model.

Interestingly, regardless of the difference in the setups and radiative transfer codes, the upper limit to the total ejecta mass is similar to that in Andreoni et al. (2020) for those omitting

the contribution from the fission fragments.⁷ Indeed, the upper limits obtained for $M_{\text{pm}} = M_d$ shown in the lower right panel of Figure 9 agree approximately with the upper limits obtained in Andreoni et al. (2020). However, we note that the agreement of the results may be a coincidence due to the fact that the model of Bulla (2019) predicts fainter emission than our simulation for the same setup of ejecta (M. Bulla 2019, private communication), while the lanthanide-poor ejecta ($Y_e = 0.3\text{--}0.4$) arranged in the polar region of the ejecta model

⁷ We note that the analytical model of the heating rate employed in Bulla (2019) approximately agrees with the heating rate employed in our models for the case in which the contribution from the fission fragments is omitted.

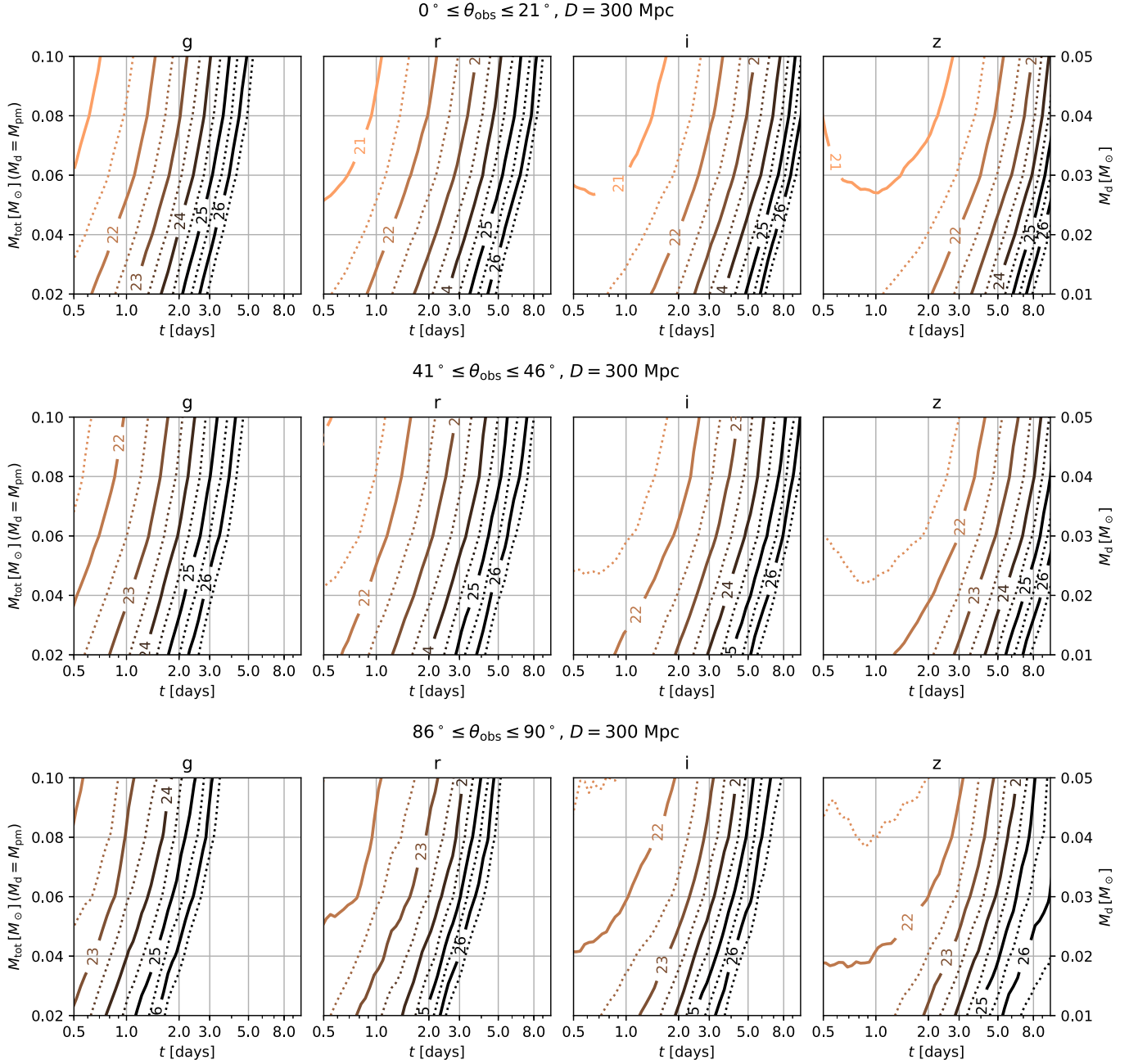


Figure 10. Required depth of the observation in the *griz*-band filters to detect the BH–NS kilonovae with $M_{\text{pm}} = M_d$. The top, middle, and bottom panels denote the results for $0^\circ \leq \theta_{\text{obs}} \leq 20^\circ$, $41^\circ \leq \theta_{\text{obs}} \leq 46^\circ$, and $86^\circ \leq \theta_{\text{obs}} \leq 90^\circ$, respectively. The hypothetical distance to the event is set to be 300 Mpc. The dotted curves denote the contours with 0.5 mag intervals. We note that the results before $t = 1$ day may not be very reliable due to lack of the opacity table for highly ionized atoms (see Tanaka et al. 2019).

in Bulla (2019) enhances the z -band emission at 3.43 days by ≈ 0.5 mag (see Appendix B).

Second, we compare our results with those of Andreoni et al. (2020) obtained by employing the 1D kilonova model of Hotokezaka & Nakar (2020). In the model of Hotokezaka & Nakar (2020), (i) a homologously expanding spherical ejecta with a single power-law density profile is employed, (ii) the opacity is given by a constant value under the gray approximation, and (iii) the light curves are calculated based on the variant of Arnett’s analytical model (Arnett 1982) with the stratified structure of the ejecta. The radioactive heating, as well as its thermalization, is computed based on a nuclear

database and by taking the dependence on the decay energy into account (see Hotokezaka & Nakar 2020 for the detail). In Andreoni et al. (2020), the models with the ejecta profile of $\rho \propto v^{-4.5}$ distributing from 0.1 to $0.4c$ are employed varying the value of gray opacity for the entire ejecta.

The upper limit to the ejecta mass in the 1D kilonova models of Hotokezaka & Nakar (2020) is weaker than that we obtained. While our results constrain the ejecta mass to be smaller than $0.06\text{--}0.07 M_\odot$ for $D = 215$ Mpc (see Figure 6), the ejecta mass is not totally constrained up to $0.1 M_\odot$ by the 1D model in Andreoni et al. (2020) for a typical value of opacity for lanthanide-rich ejecta ($\kappa \sim 10 \text{ cm}^2 \text{ g}^{-1}$;

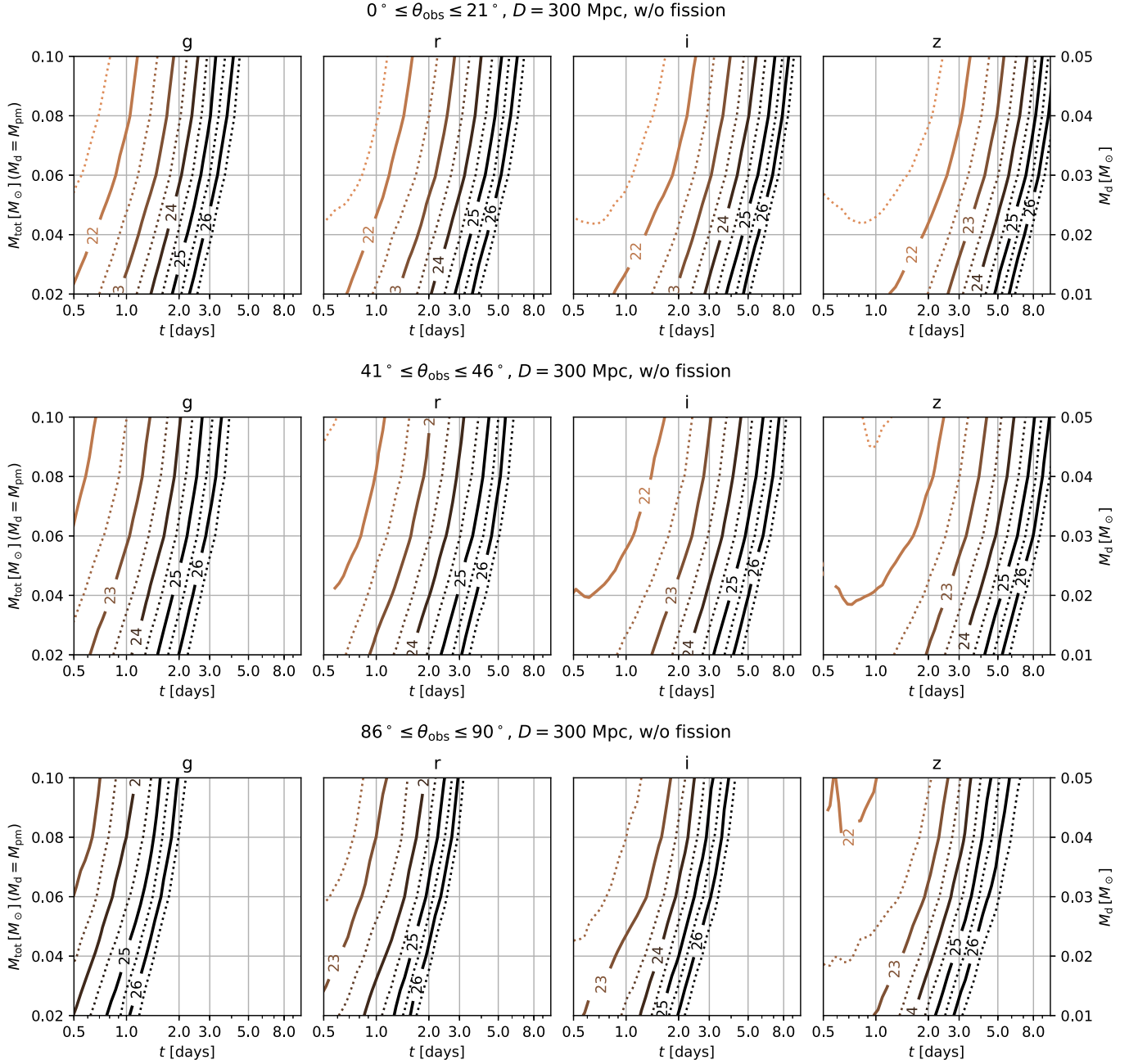


Figure 11. Same as Figure 10 but for the models without fission fragments.

Tanaka & Hotokezaka 2013). This may be due to the low effective temperature of the emission, which results from the high-velocity edge of the ejecta profile in their model. The high-velocity edge of the ejecta is set to be $0.4c$ in their model, while $0.1c$ is employed for our postmerger ejecta model. The photosphere is located at a larger radius for such a model with a high-velocity edge, and the optical emission is suppressed because the spectra are reddened. Indeed, we performed a calculation for our postmerger ejecta model with a maximum velocity twice as large as the fiducial setup, that is, $0.2c$ (see Equation (1)). We found that the z -band emission fainter by more than 1 mag is realized at 3.43 days for this model. Thus, while we employ conservative setups based on theoretical predictions obtained by numerical-relativity simulations, we could note that the constraint on the ejecta mass should depend

largely on the assumptions of ejecta profiles and microphysical models employed.

Finally, we compare our results with those of Ackley et al. (2020) obtained by employing the 2D kilonova model of Barbieri et al. (2019). Barbieri et al. (2019) considered the model with multiple ejecta components composed of the dynamical ejecta with nonspherical geometry and the postmerger ejecta with a spherical and equatorial-dominated density profile ($\propto \sin^2\theta$). The opacity of each ejecta component is given by a constant value under the gray approximation, while 15 and $5 \text{ cm}^2 \text{ g}^{-1}$ are employed for the dynamical and postmerger components, respectively. Then the luminosity is calculated by determining the ejecta region from which photons can diffuse out, which is the extension of the methods introduced by Piran et al. (2013) and Kawaguchi et al. (2016).

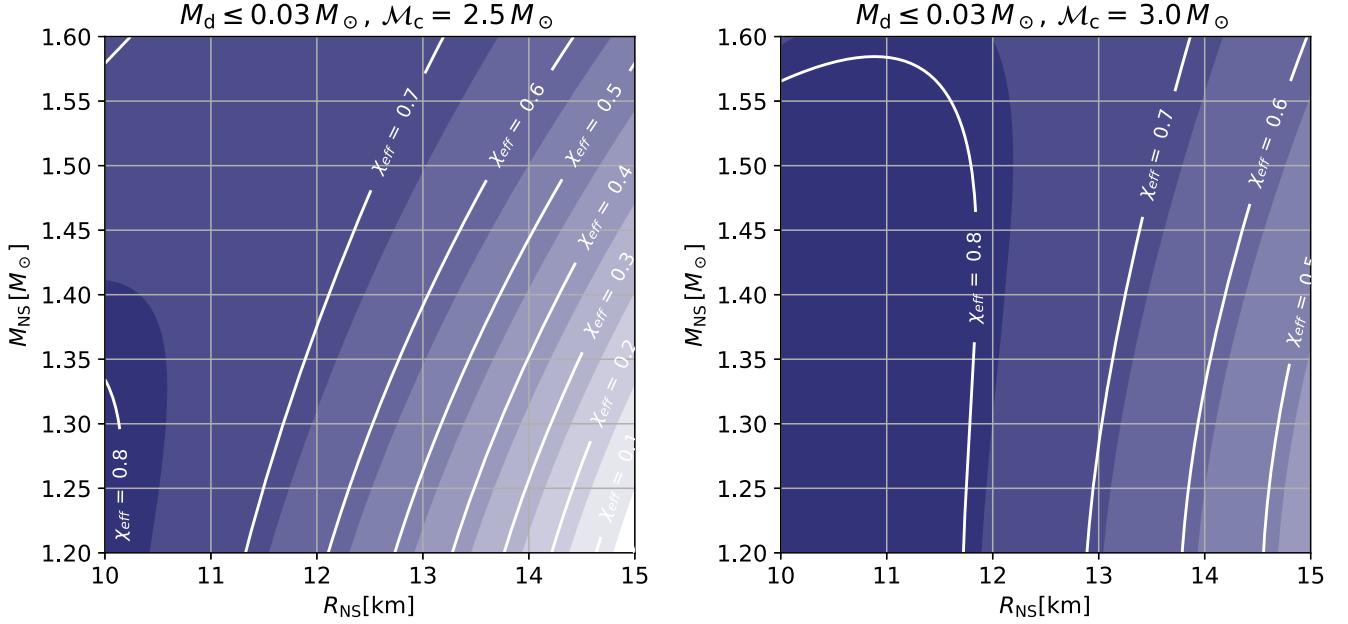


Figure 12. Allowed region of the NS mass and radius for $M_d \leq 0.03 M_\odot$ with $M_c = 2.5$ and $3.0 M_\odot$. Each white curve with an effective spin value denotes the NS mass and radius for which $M_d = 0.03 M_\odot$ is predicted by the fitting formula (Kawaguchi et al. 2016; Coughlin et al. 2017) using the corresponding value of the effective spin. The NS mass and radius are allowed only on the left side of the curve for a given upper limit to the effective spin. We note that the boundaries of the deeper-color regions are determined by $M_d - \Delta M_d = 0.03 M_\odot$ to take the estimated error of the fitting formula, ΔM_d , into account (see Kawaguchi et al. 2016 for details).

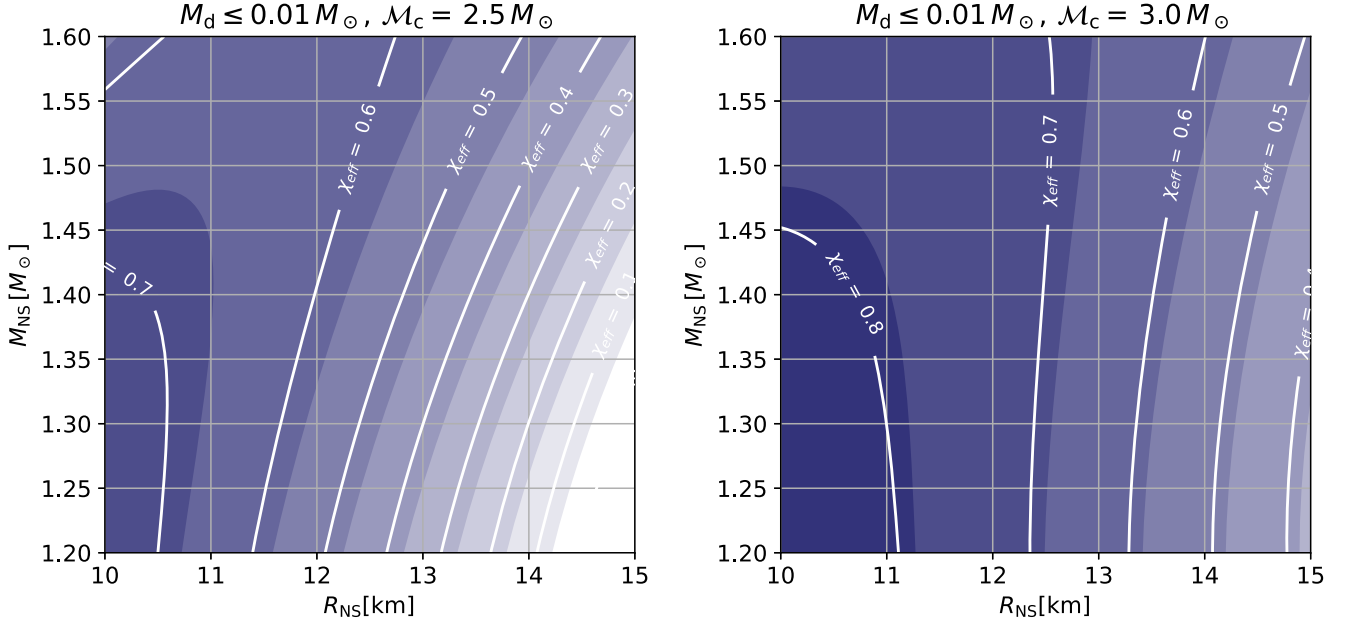


Figure 13. Same as Figure 12 but for $M_d \leq 0.01 M_\odot$.

The dynamical and postmerger ejecta are discretized in the radial and latitudinal cells, respectively, so that the viewing angle dependence of the light curves can be taken into account. The spectra are calculated by integrating the photon contribution from each discretized cell of ejecta in which blackbody emission is assumed. In their analysis, $\theta_{\text{obs}} = 30^\circ$ is assumed.

Ackley et al. (2020) concluded that $M_d \geq 0.1 M_\odot$ is excluded with high confidence, which is consistent with our results of $\theta_{\text{obs}} \leq 45^\circ$. They also showed that $M_d \geq 0.01$ and

$M_{\text{pm}} \geq 0.1 M_\odot$ are disfavored at approximately 1σ confidence. Although their results are broadly consistent with ours, they gave a slightly tighter constraint to the ejecta mass. We suspect that a relatively small value of opacity ($5 \text{ cm}^2 \text{ g}^{-1}$) employed for the postmerger ejecta is responsible for this difference (see Appendix B). This indicates that employing a realistic setup for the ejecta opacity based on the element abundances of numerical-relativity simulations and atomic line opacity data taking its wavelength and density/temperature dependence is

important to suppress the bias in the ejecta parameter estimation.

4.2. Implications of Future Observations

Figures 10 and 11 show the required depth of the observation in the *griz*-band filters to detect the BH–NS kilonovae for $M_{\text{pm}} = M_{\text{d}}$ at $D = 300$ Mpc with and without the contribution of fission fragments to the heating rate, respectively. Irrespective of the fission fragments, the emission becomes brighter at longer wavelengths; hence, a kilonova with less ejecta mass can be observed if the observations are performed in a longer wavelength (e.g., the *z* band rather than the *g* band). Also, a kilonova with the same ejecta mass can be observed in the later epoch by the same depth of the observation in a band filter with longer wavelength. Thus, an observation in the *i* or *z* band could be useful to detect the kilonova (Barnes & Kasen 2013; Tanaka et al. 2014).

Focusing on the case in which the event is observed from the polar direction ($\theta_{\text{obs}} \leq 45^\circ$), a follow-up observation deeper than 22 mag within 2 days is crucial to detect the kilonovae of $M_{\text{pm}} = M_{\text{d}} = 0.03 M_\odot$. On the other hand, if the event is observed from the equatorial direction ($\theta_{\text{obs}} \geq 70^\circ$), an observation deeper than 23 mag within 2 days is required.

4.3. Constraint on the NS Mass–Radius Relation

By combining binary parameters inferred by the GW data analysis, the constraint on the dynamical ejecta mass can be used to constrain the mass–radius relation of an NS. The chirp mass of the binary, defined by $\mathcal{M}_c = \frac{M_{\text{BH}}^3 M_{\text{NS}}^{3/5}}{(M_{\text{BH}} + M_{\text{NS}})^{1/5}}$ with the BH mass M_{BH} and NS mass M_{NS} , is a quantity that can be determined most accurately from the GW data analysis. Also, the mass ratio, $q = M_{\text{BH}}/M_{\text{NS}}$, and the so-called effective spin, $\chi_{\text{eff}} = \frac{M_{\text{BH}}}{M_{\text{BH}} + M_{\text{NS}}} \chi_{\text{BH}}$, are measured for some extent. Here χ_{BH} denotes the component of the dimensionless BH spin parallel to the orbital axis, and we assume that the NS spin is negligible (Burgay et al. 2003; Abbott et al. 2017; Tauris et al. 2017). The previous numerical simulations for BH–NS mergers show that the dynamical ejecta mass is determined approximately by these parameters and the NS radius (Kawaguchi et al. 2016). Thus, the constraint on the dynamical ejecta mass could be translated to the constraint on the NS radius if the parameters introduced above are determined by the GW data analysis. We note that a similar analysis was already performed by Coughlin et al. (2020) and Andreoni et al. (2020) focusing on the total ejecta mass, but our analysis focuses on constraining the NS mass–radius relation based on the parameters that can be obtained directly by the GW data analysis.

Employing the analytical fit of the dynamical ejecta mass (Kawaguchi et al. 2016; Coughlin et al. 2017), we calculate the allowed region of the NS mass and radius for a given chirp mass, an upper limit to the dynamical ejecta mass, and a lower limit to the effective spin. We plot the results for $M_{\text{d}} \leq 0.03 M_\odot$ in Figure 12 as an illustration. The left and right panels in Figure 12 show the cases for $M_c = 2.5$ and $3.0 M_\odot$, respectively. The NS mass and radius are constrained to the region in the contour for a given lower limit of the effective spin for $M_{\text{d}} \leq 0.03 M_\odot$. Primarily, this analysis provides the upper limit to the NS radius for a given NS mass because M_{d} becomes large as the NS radius increases. We note that the fitting formula for the dynamical ejecta mass employed here is

calibrated to the numerical-relativity simulations only for $M_{\text{NS}} \approx 1.4 M_\odot$ and $4 M_\odot \lesssim M_{\text{BH}} \lesssim 10 M_\odot$, i.e., only for $\mathcal{M}_c \approx 2.0\text{--}3.0 M_\odot$ (Kawaguchi et al. 2016).

A tighter constraint is given for a larger upper limit to the effective spin because the dynamical ejecta mass increases for the case in which the BH is spinning more rapidly. The constraint on the NS mass and radius becomes weaker as the chirp mass of the binary increases. This reflects the fact that the BH mass is a monotonically increasing function of the chirp mass for a fixed NS mass, and the dynamical ejecta mass decreases as the BH mass increases in the range of \mathcal{M}_c and M_{NS} shown in Figure 12.⁸

For $\mathcal{M}_c = 2.5 M_\odot$ (e.g., for $M_{\text{NS}} = 1.4$ and $M_{\text{BH}} = 6.5 M_\odot$), the condition of $\chi_{\text{eff}} \geq 0.6$ gives a meaningful upper limit to the NS radius ($< 12\text{--}14$ km). On the other hand, for $\mathcal{M}_c = 3 M_\odot$ (e.g., for $M_{\text{NS}} = 1.4$ and $M_{\text{BH}} = 10 M_\odot$), the NS radius can be constrained by at most $\lesssim 14$ km even if the effective spin is inferred to be larger than 0.6. Thus, a BH–NS event with a chirp mass smaller than $\lesssim 3 M_\odot$ and effective spin larger than $\gtrsim 0.5$ would be important for providing the constraint on the NS mass–radius relation.

A tighter constraint on the NS mass–radius relation can be obtained if the dynamical ejecta mass is constrained to be a smaller value. Figure 13 is the same as Figure 12 but for the case in which the dynamical ejecta is constrained to be less than $0.01 M_\odot$. For example, the NS radius is typically restricted to be smaller by ≈ 0.5 km than that for $M_{\text{d}} \leq 0.03 M_\odot$ for a given value of the lower limit to χ_{eff} . As is the case for $M_{\text{d}} \leq 0.03 M_\odot$, the NS radius up to 14 km is always allowed for $\mathcal{M}_c = 3 M_\odot$ unless χ_{eff} is inferred to be larger than 0.5. Thus, a BH–NS event with $\mathcal{M}_c \lesssim 3 M_\odot$ is also crucial to obtain a valuable constraint to the NS mass–radius relation with an upper limit of $M_{\text{d}} \leq 0.01 M_\odot$.

A more stringent constraint on the NS mass and radius can be obtained for the case in which the kilonova of a BH–NS event is observed and the range of the dynamical ejecta mass is restricted. With both upper and lower limits to the dynamical ejecta mass and effective spin, the upper and lower limits to the NS radius can be obtained presuming the accurate measurement of the chirp mass. For example, if the dynamical ejecta mass is suggested to be larger than $0.01 M_\odot$, in addition to the constraint obtained by the upper limit to the dynamical ejecta mass, the NS mass and radius are restricted in the region in Figure 13 where the effective spin is smaller than the upper limit inferred by the GW analysis. Figures 12 and 13 indicate that, to constrain the NS radius within ≈ 1 km error, constraints on the dynamical ejecta mass and effective spin with $\Delta M_{\text{d}} \lesssim 0.01 M_\odot$ and $\Delta \chi_{\text{eff}} \lesssim 0.1$ for the BH–NS event of $\mathcal{M}_c \leq 3.0 M_\odot$ are crucial.

5. Summary

In this paper, we studied the upper limit to the ejecta mass based on the upper limits to the emission obtained by the EM counterpart follow-up campaigns for the BH–NS merger candidate event S190814bv by performing radiative transfer simulations for kilonovae. In our calculation, the realistic ejecta density profile and the detailed opacity and heating rate models consistent with the numerical-relativity simulations (e.g.,

⁸ We note that the dynamical ejecta mass would be an increasing function of the BH mass for a small mass ratio $q \lesssim 3$ (Foucart et al. 2019), while q is always larger than 3 in the range of \mathcal{M}_c and M_{NS} shown in Figure 12.

Foucart et al. 2014, 2015, 2019; Metzger & Fernández 2014; Kyutoku et al. 2015, 2018; Wu et al. 2016; Siegel & Metzger 2017, 2018; Christie et al. 2019; Fernández et al. 2019; Fujibayashi et al. 2020) are employed. In addition, the temperature and opacity are evolved consistently with the radiative transfer. In this study, we found that the upper limit to the z -band emission at $t = 3.43$ days obtained by DECAM (Andreoni et al. 2020) and the upper limit to the K band at 9.2–10.5 days by VISTA (Ackley et al. 2020) give the tightest constraint on the kilonova light-curve model.

We showed that the brightness of the emission in the z band at $t = 3.43$ days depends not only on the total ejecta mass but also on the ratio between the dynamical and postmerger ejecta mass. We showed that the model with only the postmerger ejecta gives the faintest emission for $\theta_{\text{obs}} \lesssim 45^\circ$ for a given total ejecta mass, while the faintest emission for $\theta_{\text{obs}} \gtrsim 60^\circ$ is realized for the case in which 20%–50% of the ejecta is the dynamical component. We also found that the K -band emission at $t = 10.5$ days has broadly the same dependence, while the viewing angle dependence is weaker than that for the z -band emission. We found that a total ejecta mass larger than $0.1 M_\odot$ is consistent with the upper limits to the z and K bands for $D \geq 267$ Mpc or $\theta_{\text{obs}} \gtrsim 60^\circ$. For $\theta_{\text{obs}} \leq 45^\circ$ and $D = 215$ Mpc, the total ejecta mass is constrained to be less than $0.07 M_\odot$. However, these upper limits are not strong enough to indicate particular parameters of the binary. Thus, although there always exists a trade-off between the depth and the area, we recommend deeper observations than those in the current strategy to detect or obtain a tight constraint on the kilonovae at $D \gtrsim 200$ Mpc.

We also studied the upper limit to the ejecta mass, focusing on the dynamical component. For the case in which the postmerger ejecta mass is larger than the dynamical ejecta mass, and taking the contribution of the fission fragments to the heating rate into account, we found that the dynamical ejecta mass has to be smaller than 0.02 , 0.03 , and $0.05 M_\odot$ for $\theta_{\text{obs}} \leq 20^\circ$, $\theta_{\text{obs}} \leq 50^\circ$, and the entire viewing angle, respectively. We also showed that the upper limit to the dynamical ejecta mass is strongly affected by the uncertainty in the contribution of the fission fragments to the heating rate. If the contribution of the fission fragments to the heating rate is omitted, the models with a dynamical ejecta mass as large as $0.05 M_\odot$ are consistent with the upper limits to the z and K bands for $\theta_{\text{obs}} \geq 30^\circ$.

In Figures 10 and 11, we summarize the depth of observation required to detect the kilonova for a given total ejecta mass for the cases with $M_{\text{pm}} = M_{\text{d}}$. We showed that, for the case in which a BH–NS merger event is detected by GWs from the polar direction ($\theta_{\text{obs}} \leq 45^\circ$) at $D = 300$ Mpc, the iz -band observation deeper than 22 mag within 2 days after the GW trigger is crucial to detect a kilonova with a total ejecta mass of $0.06 M_\odot$ (and a dynamical ejecta of $0.03 M_\odot$). To achieve this, the EM follow-up by 4/8 m class telescopes is crucial (Nissanke et al. 2013). We note that the kilonova detection will be more feasible in the presence of the lanthanide-poor postmerger ejecta, particularly in the shorter wavelengths (e.g., in the g and z bands; see also Appendix B; e.g., Metzger & Fernández 2014; Tanaka et al. 2018; Kawaguchi et al. 2020).

We showed that the constraint on the dynamical ejecta mass can be used to constrain the mass–radius relation of an NS by combining the binary parameter inferred by the GW data analysis, such as the chirp mass and effective spin. We showed

that a BH–NS event with a chirp mass smaller than $\lesssim 3 M_\odot$ and effective spin larger than $\gtrsim 0.5$ can provide an interesting indication of the NS mass–radius relation by this analysis if the dynamical ejecta mass $\lesssim 0.03 M_\odot$ is obtained.

We thank Mattia Bulla for a valuable discussion and the cross-comparison of the radiative transfer simulation codes. Numerical computation was performed on the Cray XC40 at the Yukawa Institute for Theoretical Physics, Kyoto University, and the Sakura cluster at the Max Planck Institute for Gravitational Physics (Albert Einstein Institute). This work was supported by Grants-in-Aid for Scientific Research (JP16H02183, JP16H06342, JP17H01131, JP15K05077, JP17K05447, JP17H06361, JP15H02075, JP17H06363, 18H05859) of the JSPS and a post-K computer project (priority issue No. 9) of the Japanese MEXT.

Appendix A

The Upper Limit to the Dynamical Ejecta Mass for $M_{\text{pm}} = 0.5 M_{\text{d}}$

The upper limit to the dynamical ejecta mass becomes weaker if we allow the postmerger ejecta mass to be smaller than the dynamical ejecta mass. Indeed, for some cases of BH–NS mergers, the remnant torus mass could be comparable to the dynamical ejecta mass (see the models labeled with Q7a5 in Kyutoku et al. 2015); hence, the postmerger ejecta mass could be smaller than the dynamical one. Thus, we also explore the cases in which the postmerger ejecta mass is half of the dynamical ejecta mass ($M_{\text{pm}} = 0.5 M_{\text{d}}$).

Figure A1 is the same as Figure 7 but for the models with ($M_{\text{d}}, M_{\text{pm}} = (0.02, 0.01 M_\odot)$, $(0.03, 0.015 M_\odot)$, $(0.04, 0.02 M_\odot)$, and $(0.05, 0.025 M_\odot)$). First, we focus on the models in which the contribution from the fission fragments to the heating rate is taken into account (see the left panel). The left panel of Figure A1 shows that the models with $2M_{\text{pm}} = M_{\text{d}} \geq 0.03$ and $0.04 M_\odot$ are disfavored for $\theta_{\text{obs}} \leq 30^\circ$ and 50° , respectively. The models with $2M_{\text{pm}} = M_{\text{d}} > 0.05 M_\odot$ are disfavored for the entire viewing angle, as is the case for the model with $M_{\text{pm}} = M_{\text{d}}$. We note that the brightness of the emission for $\theta_{\text{obs}} \gtrsim 70^\circ$ is approximately the same as for the model with $M_{\text{pm}} = M_{\text{d}}$. This indicates that the emission for $\theta_{\text{obs}} \gtrsim 70^\circ$ is dominated by the emission from the dynamical ejecta.

The upper limit to the ejecta mass is weaker for the models without the fission fragments. The right panel of Figure A1 shows that, even for the case of $2M_{\text{pm}} = M_{\text{d}} = 0.05 M_\odot$, the model is marginally consistent with the upper limit to the z -band emission at $t = 3.43$ days for the entire viewing angle by omitting the contribution from the fission fragments to the heating rate.

Figure A2 is the same as Figure A1 but for the brightness of the K -band emission at $t = 10.5$ days with the upper limit obtained by VISTA (Ackley et al. 2020). As in Section 3.2, slightly weaker and tighter constraints on M_{d} are obtained for $\theta_{\text{obs}} \lesssim 45^\circ$ and $\gtrsim 45^\circ$, respectively, by the upper limit to the K -band emission than that to the z band.

Figure A3 shows the upper limit to the dynamical ejecta mass as a function of θ_{obs} for the models with $M_{\text{pm}} = 0.5 M_{\text{d}}$. A dynamical ejecta mass larger by $\approx 10\%$ – 50% is allowed for the models with $M_{\text{pm}} = 0.5 M_{\text{d}}$ than those with $M_{\text{pm}} = M_{\text{d}}$ for $\theta_{\text{obs}} \leq 60^\circ$, while approximately the same upper limits are obtained for $\theta_{\text{obs}} \geq 70^\circ$.

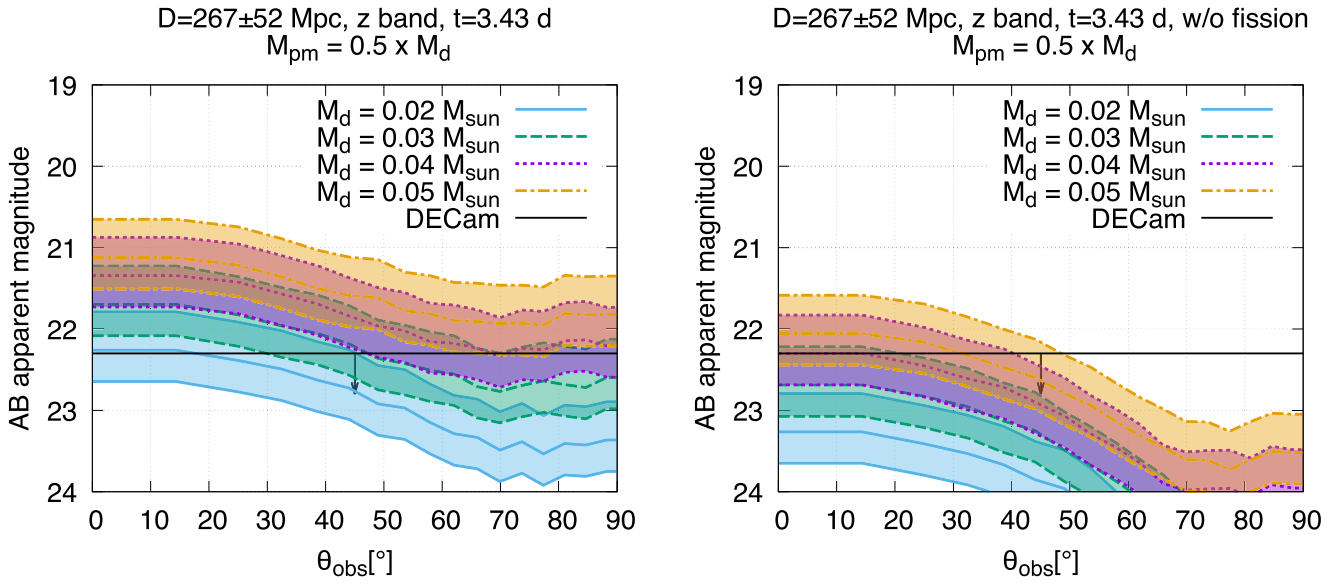


Figure A1. Same as Figure 7 but for the models with $(M_d, M_{pm}) = (0.02, 0.01 M_\odot)$; (blue solid), $(0.03, 0.015 M_\odot)$; (green dashed), $(0.04, 0.02 M_\odot)$; (purple dotted), and $(0.05, 0.025 M_\odot)$; (orange dashed-dotted). The right and left panels show the models in which the contribution from the fission fragments to the heating rate is taken into account and omitted, respectively.

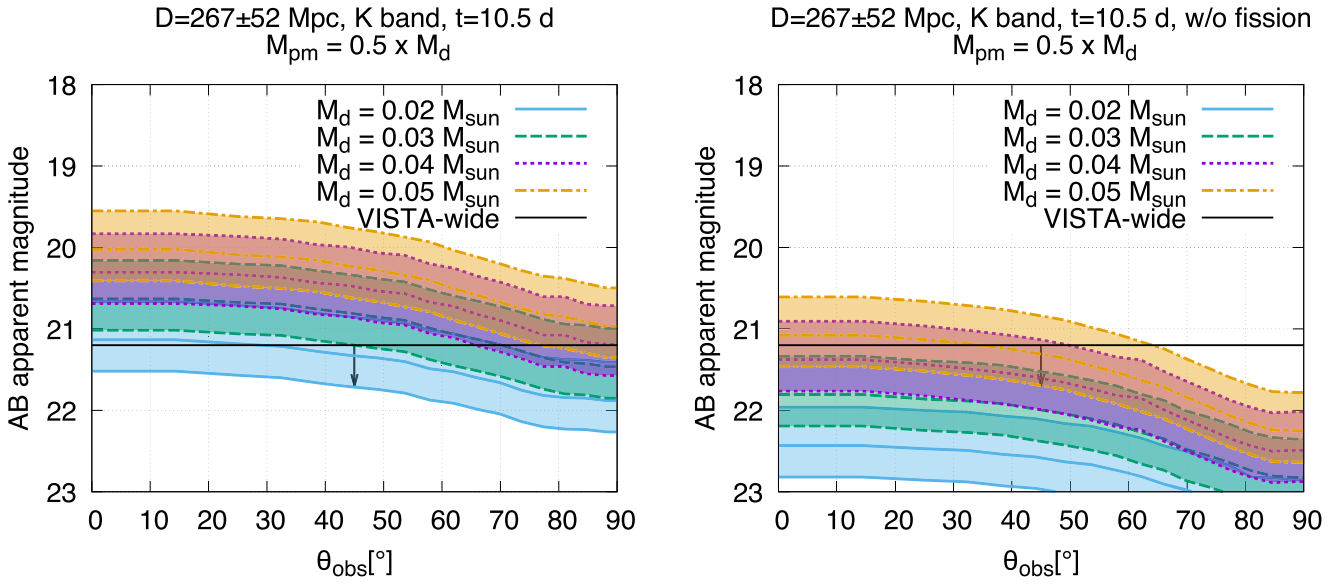


Figure A2. Same as Figure A1 but for the brightness of the K-band emission at $t = 10.5$ days with the upper limit obtained by VISTA (Ackley et al. 2020).

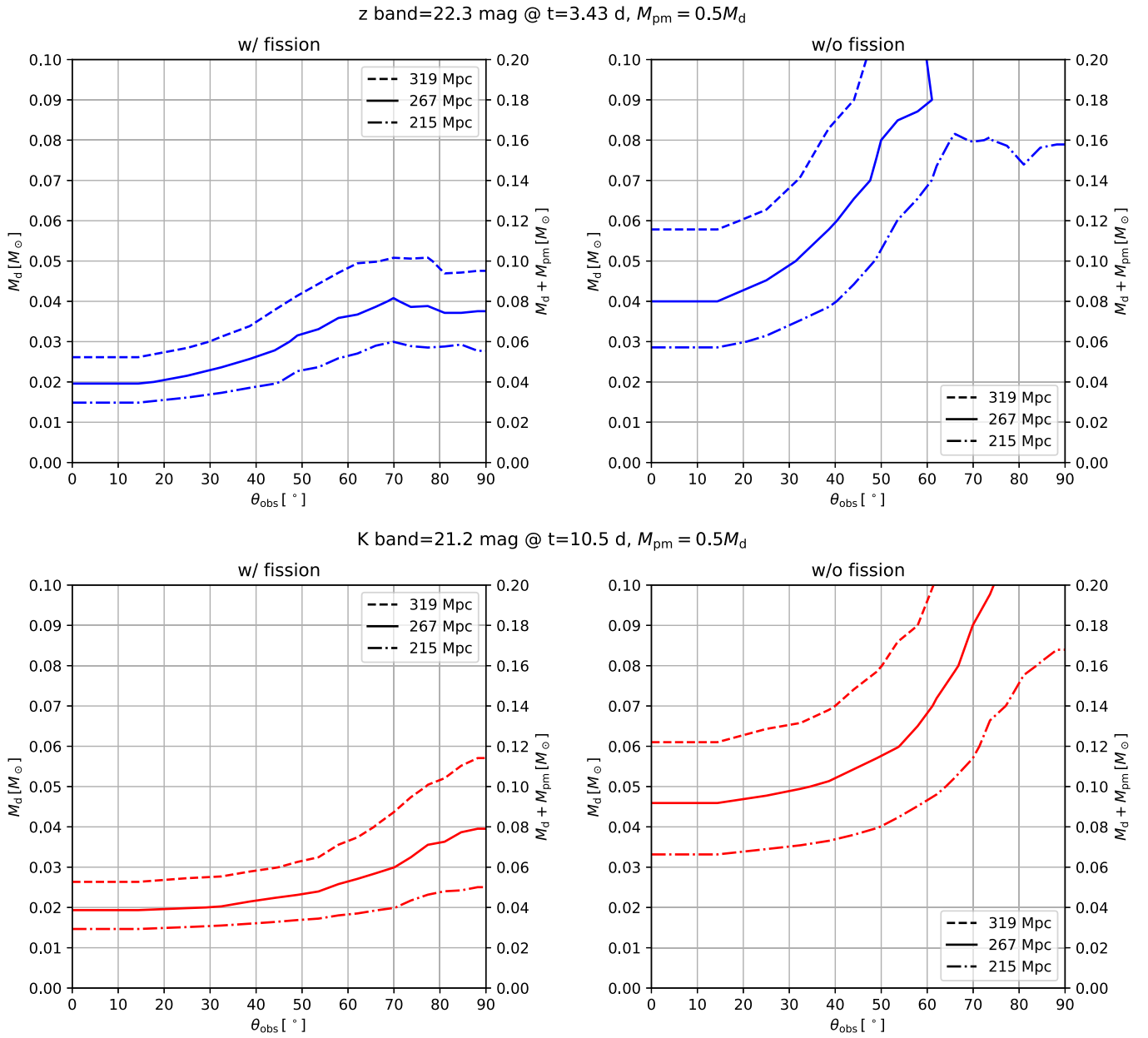


Figure A3. Same as Figure 9 but for the models with $M_{\text{pm}} = 0.5M_d$.

Appendix B High- Y_e Postmerger Ejecta

Figure B1 compares the brightness of the z-band emission at $t = 3.43$ days between the models with the lanthanide-rich ($Y_e = 0.1-0.3$) and lanthanide-poor ($Y_e = 0.3-0.4$) postmerger ejecta. A tighter upper limit to the ejecta mass is obtained for the lanthanide-poor ($Y_e = 0.3-0.4$) models than the lanthanide-rich ($Y_e = 0.1-0.3$) models. For the models with $M_{\text{pm}} = M_d$, the emission for the model that is lanthanide-poor ($Y_e = 0.3-0.4$) is brighter than ≈ 0.5 mag than that with the

lanthanide-rich ($Y_e = 0.1-0.3$) postmerger ejecta due to the low value of opacity (Tanaka et al. 2019) for $\theta_{\text{obs}} \lesssim 45^\circ$. On the other hand, the enhancement of the emission is less significant for the models with $M_{\text{pm}} = 0.5M_d$ due to a more significant contribution of the emission from the dynamical ejecta. For the cases with $M_{\text{pm}} = M_d$ and $0.5M_d$, the emission observed from $\theta_{\text{obs}} \gtrsim 70^\circ$ is approximately identical between the models with lanthanide-rich and lanthanide-poor postmerger ejecta because the emission is dominated by that from the dynamical ejecta.

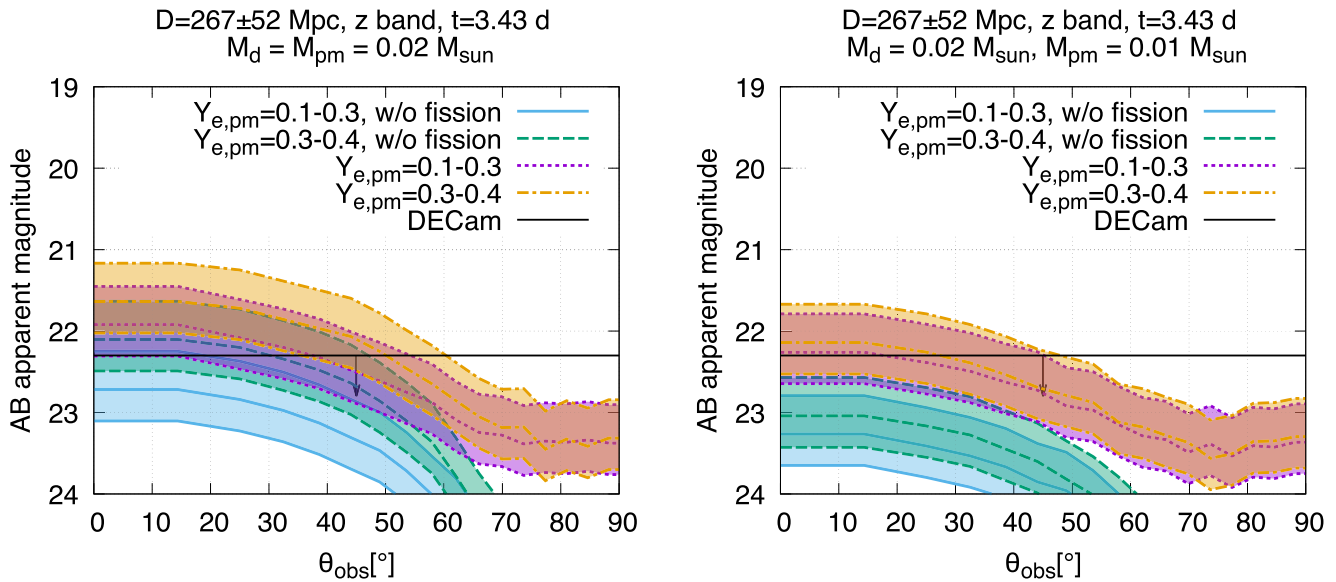


Figure B1. Comparison of the brightness of the z -band emission at $t = 3.43$ days between the models with a flat Y_e distribution of the postmerger ejecta in 0.1–0.3 and 0.3–0.4. The left and right panels show the models with $(M_d, M_{pm}) = (0.02, 0.02 M_\odot)$ and $(0.01, 0.02 M_\odot)$, respectively. Curves labeled “w/o fission” denote the results for the models in which the contribution from the fission fragments to the heating rate is omitted. The black horizontal lines in the left and right panels show the upper limits to the z -band emission at 3.43 days for S190814bv obtained by DECcam (Andreoni et al. 2020).

ORCID iDs

Masaru Shibata <https://orcid.org/0000-0002-4979-5671>

Masaomi Tanaka <https://orcid.org/0000-0001-8253-6850>

References

- Aasi, J., Abbott, B. P., Abbott, R., et al. 2015, *CQGra*, 32, 074001
- Abbott, B. P., Abbott, R., Abbott, T. D., et al. 2017, *PhRvL*, 119, 161101
- Abbott, B. P., Abbott, R., Abbott, T. D., et al. 2020, *ApJ*, 892, 3
- Acernese, F., Agathos, M., Agatsuma, K., et al. 2015, *CQGra*, 32, 024001
- Ackley, K., Amati, L., Barbieri, C., et al. 2020, arXiv:2002.01950
- Andreoni, I., Goldstein, D. A., Kasliwal, M. M., et al. 2020, *ApJ*, 890, 131
- Arnett, W. D. 1982, *ApJ*, 253, 785
- Barbieri, C., Salafia, O. S., Perego, A., Colpi, M., & Ghirlanda, G. 2019, *A&A*, 625, A152
- Barnes, J., & Kasen, D. 2013, *ApJ*, 775, 18
- Barnes, J., Kasen, D., Wu, M.-R., & Martínez-Pinedo, G. 2016, *ApJ*, 829, 110
- Bulla, M. 2019, *MNRAS*, 489, 5037
- Burgay, M., D’Amico, N., Possenti, A., et al. 2003, *Natur*, 426, 531
- Carrasco, F., & Shibata, M. 2020, *PhRvD*, 101, 063017
- Christie, I. M., Lalakos, A., Tchekhovskoy, A., et al. 2019, *MNRAS*, 490, 4811
- Coughlin, M., Dietrich, T., Kawaguchi, K., et al. 2017, *ApJ*, 849, 12
- Coughlin, M. W., Dietrich, T., Antier, S., et al. 2020, *MNRAS*, 492, 863
- Darbha, S., & Kasen, D. 2020, arXiv:2002.00299
- Dhawan, S., Bulla, M., Goobar, A., Sagués Carracedo, A., & Setzer, C. N. 2020, *ApJ*, 888, 67
- Dietrich, T., & Ujevic, M. 2017, *CQGra*, 34, 105014
- Eastman, R. G., & Pinto, P. A. 1993, *ApJ*, 412, 731
- Etienne, Z. B., Liu, Y. T., Shapiro, S. L., & Baumgarte, T. W. 2009, *PhRvD*, 79, 044024
- Fernández, R., & Metzger, B. D. 2013, *MNRAS*, 435, 502
- Fernández, R., Tchekhovskoy, A., Quataert, E., Foucart, F., & Kasen, D. 2019, *MNRAS*, 482, 3373
- Foucart, F., Deaton, M. B., Duez, M. D., et al. 2014, *PhRvD*, 90, 024026
- Foucart, F., Duez, M. D., Kidder, L. E., et al. 2019, *PhRvD*, 99, 103025
- Foucart, F., Hinderer, T., & Nissanke, S. 2018, *PhRvD*, 98, 081501
- Foucart, F., O’Connor, E., Roberts, L., et al. 2015, *PhRvD*, 91, 124021
- Fujibayashi, S., Kiuchi, K., Nishimura, N., Sekiguchi, Y., & Shibata, M. 2018, *ApJ*, 860, 64
- Fujibayashi, S., Shibata, M., Wanajo, S., et al. 2020, arXiv:2001.04467
- Gomez, S., Hosseinzadeh, G., Cowperthwaite, P. S., et al. 2019, *ApJL*, 884, L55
- Hotokezaka, K., Kiuchi, K., Kyutoku, K., et al. 2013, *PhRvD*, 87, 024001
- Hotokezaka, K., & Nakar, E. 2020, *ApJ*, 891, 152
- Just, O., Bauswein, A., Pulpillo, R. A., Goriely, S., & Janka, H. T. 2015, *MNRAS*, 448, 541
- Kasen, D., Badnell, N. R., & Barnes, J. 2013, *ApJ*, 774, 25
- Kasen, D., Fernandez, R., & Metzger, B. 2015, *MNRAS*, 450, 1777
- Kasen, D., Thomas, R. C., & Nugent, P. 2006, *ApJ*, 651, 366
- Kawaguchi, K., Kyutoku, K., Nakano, H., et al. 2015, *PhRvD*, 92, 024014
- Kawaguchi, K., Kyutoku, K., Shibata, M., & Tanaka, M. 2016, *ApJ*, 825, 52
- Kawaguchi, K., Shibata, M., & Tanaka, M. 2018, *ApJL*, 865, L21
- Kawaguchi, K., Shibata, M., & Tanaka, M. 2020, *ApJ*, 889, 171
- Kiuchi, K., Sekiguchi, Y., Kyutoku, K., et al. 2015, *PhRvD*, 92, 064034
- Kulkarni, S. R. 2005, arXiv:astro-ph/0510256
- Kuroda, K. 2010, *CQGra*, 27, 084004
- Kurucz, R. L., & Bell, B. 1995, Atomic Line List (Cambridge, MA: Smithsonian Astrophysical Observatory)
- Kyutoku, K., Ioka, K., Okawa, H., Shibata, M., & Taniguchi, K. 2015, *PhRvD*, 92, 044028
- Kyutoku, K., Kiuchi, K., Sekiguchi, Y., Shibata, M., & Taniguchi, K. 2018, *PhRvD*, 97, 023009
- Li, L.-X., & Paczynski, B. 1998, *ApJL*, 507, L59
- Lippuner, J., Fernández, R., Roberts, L. F., et al. 2017, *MNRAS*, 472, 904
- Lovelace, G., Duez, M. D., Foucart, F., et al. 2013, *CQGra*, 30, 135004
- Metzger, B. D., & Fernández, R. 2014, *MNRAS*, 441, 3444
- Metzger, B. D., Martínez-Pinedo, G., Darbha, S., et al. 2010, *MNRAS*, 406, 2650
- Most, E. R., & Philippov, A. A. 2020, *ApJ*, 893, 6
- Nissanke, S., Kasliwal, M., & Georgieva, A. 2013, *ApJ*, 767, 124
- Paczynski, B. 1991, *AcA*, 41, 257
- Piran, T., Nakar, E., & Rosswog, S. 2013, *MNRAS*, 430, 2121
- Rosswog, S. 2005, *ApJ*, 634, 1202
- Rosswog, S., Piran, T., & Nakar, E. 2013, *MNRAS*, 430, 2585
- Ruiz, M., Shapiro, S. L., & Tsokaros, A. 2018, *PhRvD*, 98, 123017
- Shibata, M., & Taniguchi, K. 2008, *PhRvD*, 77, 084015
- Siegel, D. M., & Metzger, B. D. 2017, *PhRvL*, 119, 231102
- Siegel, D. M., & Metzger, B. D. 2018, *ApJ*, 858, 52
- Singer, L. P., Kasliwal, M. M., Coughlin, M. W., et al. 2019, GCN Circular, 25381, 1
- Srivastav, S., Huber, M., Smartt, S. J., et al. 2019, GCN Circular, 25417, 1
- Tanaka, M., & Hotokezaka, K. 2013, *ApJ*, 775, 113
- Tanaka, M., Hotokezaka, K., Kyutoku, K., et al. 2014, *ApJ*, 780, 31
- Tanaka, M., Kato, D., Gaigalas, G., et al. 2018, *ApJ*, 852, 109
- Tanaka, M., Kato, D., Gaigalas, G., & Kawaguchi, K. 2019, arXiv:1906.08914
- Tanaka, M., Utsumi, Y., Mazzali, P. A., et al. 2017, *PASJ*, 69, 102
- Tauris, T. M., Kramer, M., Freire, P. C. C., et al. 2017, *ApJ*, 846, 170

The LIGO Scientific Collaboration and the Virgo Collaboration 2019, GCN
Circular, [25333](#), [1](#)
Villar, V. A., Guillochon, J., Berger, E., et al. 2017, [ApJL](#), [851](#), [L21](#)
Wanajo, S. 2018, [ApJ](#), [868](#), [65](#)

Wanajo, S., Sekiguchi, Y., Nishimura, N., et al. 2014, [ApJL](#), [789](#), [L39](#)
Wu, M.-R., Fernández, R., Martínez-Pinedo, G., & Metzger, B. D. 2016,
[MNRAS](#), [463](#), [2323](#)
Zhu, Y., Wollaeger, R. T., Vassh, N., et al. 2018, [ApJL](#), [863](#), [L23](#)